Available online at www.sciencedirect.com
SCIENCE DIRECT®
Journal of Geodynamics 39 (2005) 277–316
JOURNAL OF GEODYNAMICS
http://www.elsevier.com/locate/jog

Constraints on the composition and thermal structure of the upper mantle beneath NW Turkey: Evidence from mantle xenoliths and alkali primary melts

E. Aldanmaz [a,*], A. Gourgaud [b], N. Kaymakcı [c]

[a] *Department of Geology, University of Kocaeli, Izmit 41040, Turkey*
[b] *Universite Blaise Pascal, Department de Geologie, CNRS-UMR 6524, OPGS, CRV, rue Kessler, Clermont-Ferrand, Cedex 63038, France*
[c] *Department of Geology, Middle East Technical University, Ankara 06531, Turkey*

Received 12 July 2004; received in revised form 4 January 2005; accepted 21 January 2005

Abstract

Ultramafic xenoliths entrained in the Late Miocene alkali basalts and basanites from NW Turkey include refractory spinel-harzburgites and dunites accompanied by subordinate amount of spinel-lherzolites. Whole-rock major element and mineral chemical characteristics indicate that the xenoliths are mostly the solid residues of varying degrees of partial melting (∼3 to ∼15%), but some have mineral chemical signatures reflecting processes of melt/rock interaction. The mineral compositions of the undisturbed xenoliths have been used to estimate temperatures and, where possible, pressures of equilibration, and to construct a geothermal framework to interpret the thermal structure of the upper mantle beneath the region at the time of basaltic melt extraction. Most of the peridotite xenoliths have chemically homogeneous mineral phases reflecting ambient equilibrium pressure–temperature conditions. The combination of results from Ca-in-orthopyroxene geothermometer and Ca-in-olivine geobarometer yields pressure–temperature estimates for spinel-peridotites that fall in experimentally determined spinel-lherzolite field in CaO–Fe–MgO–Al_2O_3–SiO_2–Cr_2O_3 (CFMASCr) system. These pressure–temperature data sets have been used to construct the Late Cenozoic geotherm of NW Turkey, which defines a depth-temperature array from about 1.4 GPa at 810 °C to 2.1 GPa at 1180 °C. Extrapolation of this array to the adiabatic upwelling curve of normal temperature asthenospheric mantle indicates an apparent lithospheric thickness of ∼80 km. The geothermal gradient of NW Turkey is only slightly higher than that of the conventional conductive models (∼90 mW m^{-2}) and may be interpreted as being a consequence of the thermal perturbation by the heat input into the relatively thin mantle

* Corresponding author.
E-mail address: ercan.aldanmaz@dunelm.org.uk (E. Aldanmaz).

0264-3707/$ – see front matter
doi:10.1016/j.jog.2005.01.002

lithosphere via the passage and emplacement of magma(s). In contrast, the calculations, based on the melt products of experimental phase equilibria, show that the compositions of the host magmas precipitating the most magnesian olivine (with 88.5 to 91.4% forsterite; Mg_2SiO_4) phenocrysts of alkaline melts reveal significantly higher anhydrous liquidus temperatures that range from about 1290 to 1410 °C. The results are inconsistent with melt generation by either deep-seated thermal anomalies associated with mantle plumes ($T_p > 1450$ °C) or melting of thermally perturbed (wet) mantle lithosphere, but are consistent with the adiabatic upwelling of normal temperature ($T_p \sim 1300$ °C) mantle asthenosphere probably along the lithospheric scale major shear zones.

Keywords: Upper mantle; NW Turkey; Thermal evolution; Spinel-peridotite xenoliths; Alkali primary melts

1. Introduction

The variation in temperature with pressure in the upper mantle cannot be directly measured and, in most cases, is to be inferred from equilibrium conditions of mantle phases. The most direct indication of mantle temperatures is provided either by mantle-derived ultramafic nodules that were brought up by rapidly erupted basaltic melts of mantle origin or by defining the liquidus temperatures of eruptive products and comparing these temperatures with knowledge of the depth of origin. Ultramafic xenoliths from basaltic extrusions in continental settings provide important information on the composition, thermal state and evolution of the uppermost mantle, and the information deduced from the study of xenoliths can directly be compared with the results obtained by geophysical means. Thus, ultramafic xenoliths have been the subject of numerous mineralogical, petrological, geochemical and geothermal studies in mantle geodynamics (Frey and Green, 1974; Frey and Prinz, 1978; Maaloe and Aoki, 1977; O'Reilly and Griffin, 1985; Werling and Altherr, 1997). In recent years, lithosphere profiles have been constructed at several localities based on thermal, geophysical and petrological data with a combination of xenolith-constrained geothermal gradient for the lower crust and uppermost mantle (O'Reilly and Griffin, 1985; Ionov et al., 1998; Rudnick et al., 1998; Stern et al., 1999; Griffin et al., 2003).

NW Turkey is an active continental extensional shear zone that is characterized by relatively high surface heat flow and thermal uplift. Extension-related tectonic and magmatic activity is considered to have taken place in relation with the lithospheric thinning and asthenospheric upwelling (Aldanmaz et al., 2000). In this region, ultramafic xenoliths have been found at several localities within the alkali basalt occurrences that document mantle melting episodes during the Late Miocene (Fig. 1). Compositional variation in basaltic lavas throughout the lava sequences is limited as the volcanic rocks are generally alkaline basalt and basanite occurring as lava flows with OIB-type (or mid-plate) major-trace element and radiogenic isotope signatures (Yilmaz and Polat, 1998; Aldanmaz et al., 2000; Aldanmaz, 2002). The xenoliths erupted in alkaline magmas include refractory spinel-harzburgites and dunites accompanied by minor amount of relatively fertile spinel-lherzolites. As a whole these xenolith suits are considered to represent the uppermost mantle layer (<100 km).

In this contribution we aimed to constrain, using mineral chemistry, the recent thermal evolution of the uppermost mantle beneath NW Turkey as recorded by the equilibrium temperatures and pressures of peridotite xenoliths and to compare these results with temperatures calculated from the steady state mantle geotherm and also with the liquidus temperatures of mantle-derived primary melts, i.e. magmas precipitating the most magnesian olivine (e.g. with 88.5–91.4% forsterite; Mg_2SiO_4) phenocrysts. Such a

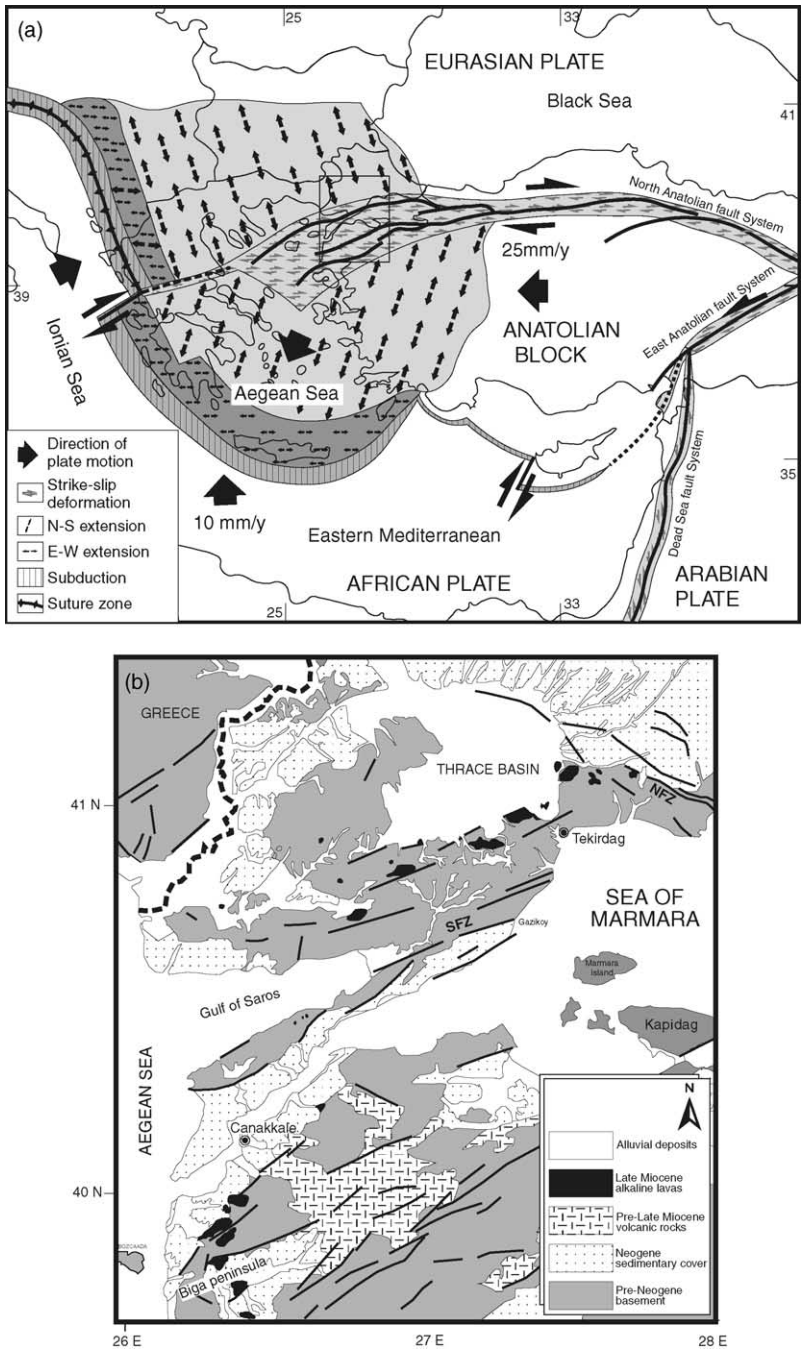

Fig. 1. (a) Map showing the plate reconstruction of eastern Mediterranean. (b) Map of NW Turkey showing the distribution of the xenolith-bearing alkaline volcanic products and the main eruption centers.

comparison is considered reasonable as the xenoliths are likely to reflect ambient pressure and temperature conditions existing in the upper mantle provided that the basaltic volcanism that brought the xenoliths to the surface are sufficiently young (<11 Ma). An additional requirement is that the upper mantle xenoliths be hosted in rapidly erupted magmas to prevent re-equilibration. Mantle-derived xenolith-bearing alkaline basaltic magmas are generally believed to have erupted quickly due to rapid transport to the surface, so that mineral composition of xenoliths probably reflect ambient pressure and temperature conditions of the source mantle before they were entrained into the host magma. Resorbed spinel crystals within the peridotite xenoliths from the alkaline volcanic rocks of NW Turkey may indicate a similar rapid transport of the xenolith-bearing magmas to the surface, but there are evidences for re-equilibration between the xenoliths and the host magmas as some of the xenoliths exhibit significant intra-grain compositional variation. We, therefore, selected samples, which are chemically homogeneous and more likely equilibrated under ambient *P–T* condition within the upper mantle.

2. Geological background

The Neogene-Quaternary tectonic evolution of NW Turkey has been largely influenced by the development of a number of strike-slip fault systems resulted from the collision of the African and Arabian plates with the Eurasian plate. The main collision that took place between the Anatolian and Arabian plates along the Bitlis–Zagros suture zone is assumed to cause the major shortening and uplift in Eastern Anatolia and the westward extrusion of the wedge-shaped Anatolian microplate as a buoyant continental sliver. The internal deformation produced within the Anatolian plate as a result of this collision involved both internal imbrication, leading to ophiolite obductions and formation of numerous strike-slip faults. The development of the latter may have been influenced by lateral variations of lithospheric rheology and the pre-existing structural framework.

The westward escape of the Anatolian microplate is accommodated by two major strike-slip faults: the right-lateral strike-slip along the North Anatolian Fault (NAF) and the left-lateral strike-slip along the East Anatolian Fault (EAF). The effect of the major, dextral, E–W trending strike-slip activity along the NAF was that the movement of the Anatolian microplate relative to the Eurasian plate changed from westwards to south-westwards with changing the deformation patterns of the fault from pure strike-slip along its eastern and central segments into a combination of right lateral and extensional mechanisms along the western segment (Fig. 1a). This led to right-lateral transtensional tectonics associated with a combination of mechanisms, including pure strike-slip along the NAF and pure extension in Greece and western Turkey. The combined effect of these two tectonic stresses generated a number of pull-apart basins in NW Turkey during the Late Miocene onwards.

The Thrace basin, one of the most important structural features of NW Turkey, is a large triangular-shaped Tertiary basin located at the junction of several other basins; the Black Sea basin is located to the northeast, the Sea of Marmara basin to the southeast, and the Aegean Basin to the southwest (Fig. 1b). Its infill comprises sedimentary rocks of Middle Eocene to Recent age, the total thickness of which has been estimated to be more than 9 km (Turgut et al., 1991; Perinçek, 1991). Sedimentary thickness variations indicate a general N–NE thinning trend. The basin is flanked predominantly by metamorphic rocks of the Strandja Massif in the north.

Structural data from the Thrace Basin are very limited because of an extensive Plio-Quaternary sedimentary cover. Most of our knowledge on basin structure comes from seismic studies and borehole data

(Turgut et al., 1991; Perinçek, 1991). Two major dextral strike-slip fault zones in the basin have been defined to form the triangular basin geometry. One of these zones extends NW–SE and borders the northern margin of the basin, and the other extends NE–SW and borders the southern margin of the basin. Both zones seem to converge at the eastern margin of the basin beneath the Sea of Marmara.

The northern fault zone consists of two sub-parallel segments that can only be mapped in the subsurface through drilling and multi-channel reflection seismic data (Turgut et al., 1991). The second fault zone bordering the southern margin of the basin is considered to represent the northwestern strand of the NAF zone. The relative right-lateral strike-slip motion along this fault has caused significant uplift and deformation on the southern margin of the basin. Turgut et al. (1991) used the sedimentary record along the southern margin of the Thrace basin to suggest a Late Miocene to Early Pliocene age for the development of the fault zone.

Extensive volcanic activity has characterized the Thrace region since the Early Miocene period (e.g. Yilmaz and Polat, 1998). This activity started with a widespread acid-intermediate, calc-alkaline volcanism and was followed by the late stage eruption of locally developed mafic alkaline products. The latter activity, which is the main subject of this study, is characterized by a number of small isolated lava flows with a 100 m of maximum thickness. The alkaline volcanic field lies mainly to the southern margin of the Thrace basin as the eruption centers are linearly distributed along this margin. The lavas erupted along NNE–SSW trending strike-slip faults that form the southernmost border of the triangle-shaped Thrace basin (Fig. 1b). The available radiometric dates yield an Upper Miocene age (11.68 ± 0.25 to 6.47 ± 0.47 Ma) for the alkaline volcanic rocks of the region (Ercan et al., 1995). The eruptive alkaline products from the Thrace volcanic field are mainly made up of olivine-phyric or aphyric lava flows that contain a large amount of mantle-derived peridotite xenoliths.

Compilation of geophysical data from earthquake seismology and quarry blast experiments reveals *Pn* velocities of 7.9 and 8.0 km s^{-1} for the uppermost mantle beneath NW Turkey and the entire Aegean region, respectively (e.g. Panagiotopoulos and Papazacos, 1985; Horasan et al., 2002), which are lower than the worldwide average continental upper mantle *Pn* velocity of 8.1 km s^{-1} (Mooney and Braile, 1989). Average heat flow density values across NW Turkey are also moderately elevated (70–90 mW m^{-2}), in comparison with 40–50 mW m^{-2} in the neighboring Black Sea basin and 30–40 mW m^{-2} in southern Turkey (Ilkisik, 1995; Pfister et al., 1998; Göktürkler et al., 2003). However, the average heat flow values, although may locally reach up to 150 mW m^{-2} due to the effects of hydrothermal fault discharge and groundwater circulation originating in adjacent highlands, are much lower than those of many active continental extensional settings such as Kenya and Rio Grande rifts, the Rhine graben and Basin and Range province that typically exceed 100 mW m^{-2}. Magnetotelluric data in much of NW Turkey have shown relatively low resistivity (>75 Ω m) beneath the base of the crust (Bayrak et al., 2004). This may indicate a possible high temperature (∼800 °C) and the presence of underplated melts at crust-mantle transition.

3. Analytical data

Only fresh xenoliths with lack signs of corrosion by host basalts were chosen for analyses. Whole-rock major oxide analyses for both the peridotite xenoliths and the host lavas were measured at the ACME analytical laboratories at Vancouver. Rock powders were first fused to ensure dissolution and then dissolved in hot HF and HNO_3 to prepare the solutions from which the element abundances were

determined using ICP-AES. Loss on ignition (LOI) was determined by heating a separate aliquot of rock powder. Whole-rock major element data for the mantle xenoliths are given in Table 1 .

Polished thin-sections of the alkaline volcanic rocks and some peridotite xenoliths were prepared at the University of Durham and were carbon coated at the University of Edinburgh. Analyses of constituent mineral phases from representative samples of both xenoliths and host lavas were performed at Edinburgh on a Cameca CAMEBAX electron microprobe using natural minerals as standards. Operating procedures were ~20 kV acceleration voltage, beam current ~20 nA, 30 s. pk count, 15 s. b/g count, 1 mm^2 spot size and a 25 mm^2 retard beam size. The application of Ca-in-olivine geobarometer (Köhler and Brey, 1990) requires very careful analyses of Ca of olivine as its concentration is about 0.03 wt.% CaO . The analysis of CaO was carried out with beam current of 100 nA and counting time 100 s. The precision of analyses was 3% relative. The detection limit was at about 0.004 wt.% Ca. All reported CaO values in olivines determined with this special analysis are averages of 5-point analyses of several grain cores.

An additional set of samples from both the alkaline lavas and the peridotites were analyzed using a Cameca CAMEBAX electron microprobe at the Blaise Pascal University, Clermont-Ferrand with operating conditions of 15 kV accelerating voltage, 10–12 nA current and 10 s counting time per each element.

4. Characteristics of the host lavas and peridotite xenoliths

The alkaline volcanic field of NW Turkey comprises a number of sub-horizontal lava flows lying mostly on the localized extensional basins formed in association with the transtensional tectonic regime of the region (Fig. 1b). The lavas have an irregular base and show development of soil horizons. Lava moraines are observed between the individual flows and well-developed columnar jointing is observed near the eruptive centers. The volcanic rock samples are extremely fresh with only a few showing incipient alteration of olivine phenocrysts along rims and interior cracks upon microscopic investigations. They consist of a fine-grained to glassy matrix with small to medium-sized (<5 mm) phenocrysts of olivine and clinopyroxene. Total phenocryst contents are variable, generally ranging from <3 (aphyric) to 15% (weakly porphyritic), but the majority of the rocks are aphyric. The xenolith-bearing lavas are very fine-grained alkali basalts and basanites containing phenocrysts of olivine ($Fo_{83–91}$) and less clinopyroxene ($Wo_{43–49}$) in a fine-grained groundmass containing granular olivine ($Fo_{76–89}$), plagioclase laths ($An_{65–73}$) and intersertal glass. Some of the magnesian samples have abundant equant to prismatic phenocrysts of olivine up to 2–4 mm in diameter. With declining content of MgO in the rock the phenocrysts became smaller. In rocks with less than ~12 wt.% MgO most olivines are <1 mm in size and the rocks are olivine microphyric or aphyric. Most glassy rocks have phenocrysts of equant to elongate-skeletal olivine with included or attached oxide phases in a dark brown glass. Plagioclase phenocrysts are absent in all rocks from the alkaline suites.

The previously published radiometric dates (K–Ar and Ar–Ar) show that the alkaline volcanic activity in the area lasted from 11.48 ± 0.40 to 6.47 ± 0.47 Ma (Ercan et al., 1995). The results of geochemical and ^{40}Ar–^{39}Ar whole-rock basalt groundmass analyses in more recent studies, however, indicate that the major volume of xenolith-bearing alkaline lavas of NW Turkey spans ~3.5 million year (11.68 ± 0.25 to 8.03 ± 0.19 Ma) of episodic volcanic activity and includes the entire compositional spectrum recognized in the alkaline suite (Aldanmaz et al., 2000; Aldanmaz et al., submitted manuscript).

Ultramafic xenoliths and discrete megacrysts are sporadically found in alkali lava flows in a number of localities within the Thrace volcanic field (Fig. 1b). The xenoliths are subangular to angular and have

Table 1
Petrographic and whole-rock major oxide data for the peridotite xenoliths from NW Turkey

Sample numbers	XE7A	XE2	XE2C	XE2B	XE7B	XE1B	XE11	XE1A	XE14	XE2A	XE13A	XE10
Rock type	Lhz.	Lhz.	Lhz.	Lhz.	Lhz.	Lhz.	Lhz.	Lhz.	Lhz.	Lhz.	Lhz.	Lhz.
Modal mineralogy												
Oliv	59.1	58.4	59.2	67.3	68.5	69.3	70.9	71.3	71.6	70.2	70.8	72.7
Opx	24.9	25.7	26.7	20.5	19.3	20.3	19.1	19.4	19.3	20.7	21.1	21.2
Cpx	12.2	12.8	11.1	10.1	10.1	8.2	8.1	7.2	7.1	7.0	6.1	5.0
Sp	3.8	3.1	3.0	2.1	2.1	2.2	1.9	2.1	2.0	2.1	2.0	1.1
Major oxid												
SiO_2	47.21	47.21	44.94	44.41	44.17	44.13	44.39	44.49	44.44	44.31	43.84	43.44
TiO_2	0.07	0.09	0.08	0.07	0.06	0.07	0.06	0.07	0.07	0.07	0.06	0.05
Al_2O_3	3.85	3.91	3.67	2.86	2.66	2.47	2.50	2.47	2.48	2.47	2.31	1.90
Fe_2O_3	7.56	7.42	8.59	8.68	8.27	7.52	7.56	7.61	7.56	7.63	7.78	7.88
MnO	0.10	0.12	0.12	0.11	0.11	0.12	0.11	0.11	0.12	0.11	0.10	0.12
MgO	37.87	36.11	38.58	40.41	41.17	41.79	41.91	42.13	41.89	41.83	42.65	43.52
CaO	3.01	3.02	2.81	2.35	2.31	2.26	2.25	2.18	2.24	2.18	2.05	1.84
Na_2O	0.24	0.36	0.34	0.26	0.20	0.14	0.15	0.15	0.14	0.13	0.11	0.08
K_2O	0.05	0.04	0.03	0.05	0.04	0.05	0.04	0.06	0.04	0.04	0.04	0.05
P_2O_5	0.01	0.01	0.01	0.01	0.01	0.01	0.01	0.01	0.01	0.01	0.01	0.01
L.O.I.	0.63	1.10	0.09	1.03	0.68	0.75	1.15	1.37	0.80	0.83	0.74	1.03
Total	100.60	99.39	99.26	100.24	99.69	99.31	100.12	100.65	99.78	99.61	99.56	99.62
$Mg\#_{WR}$	0.909	0.906	0.899	0.901	0.908	0.916	0.917	0.916	0.916	0.917	0.916	0.916
$Mg\#_{ol}$	0.896	0.897	0.898	0.899	0.902	0.903	0.903	0.905	0.904	0.905	0.909	0.906
$Cr\#_{sp}$	0.126	0.128	0.130	0.133	0.189	0.199	0.227	0.238	0.252	0.263	0.284	0.293
$Mg\#_{sp}$	0.783	0.765	0.765	0.763	0.735	0.736	0.733	0.712	0.714	0.717	0.696	0.697
F (extent of melting) (%)[a]	3.28	3.43	3.59	3.84	7.33	7.81	9.23	9.61	10.19	10.57	11.38	11.77

Table 1 (*Continued.*)

Sample numbers	XE13	XE13B	XE8	XE5	XE4	XE3	XE1	XE6	XE7	XE6A	XE6B
Rock type	Hzb.	Hzb.	Hzb.	Hzb.	Hzb.	Hzb.	Hzb.	Hzb.	Dunite	Dunite	Dunite
Modal mineralogy											
Oliv	73.8	75.7	77.5	77.3	76.8	78.0	78.8	80.7	95.3	95.6	95.7
Opx	21.0	18.4	17.4	17.4	19.1	16.9	17.1	16.2	2.7	2.4	3.3
Cpx	4.1	4.1	4.1	4.0	3.1	3.9	3.1	2.0			
Sp	1.1	1.8	1.0	1.3	1.0	1.2	1.0	1.1	2.0	2.0	1.0
Major oxid											
SiO_2	44.18	42.68	41.87	42.21	42.71	43.54	42.38	38.99	42.68	42.54	42.39
TiO_2	0.06	0.04	0.02	0.06	0.02	0.04	0.03	0.02	0.02	0.03	0.01
Al_2O_3	1.77	1.49	1.11	1.24	0.96	0.91	0.85	0.83	0.77	0.78	0.81
Fe_2O_3	8.18	8.14	7.53	9.76	8.43	8.22	8.36	9.72	8.38	8.34	8.42
MnO	0.13	0.13	0.13	0.14	0.11	0.12	0.12	0.13	0.12	0.10	0.12
MgO	43.41	44.98	45.96	44.70	44.96	44.75	45.91	47.74	46.01	46.74	46.57
CaO	1.78	1.54	1.17	1.13	0.89	1.07	0.93	0.69	0.78	0.71	0.76
Na_2O	0.14	0.05	0.01	0.04	0.02	0.04	0.01	0.01	0.01	0.01	0.01
K_2O	0.05	0.03	0.07	0.04	0.03	0.03	0.03	0.12	0.03	0.11	0.07
P_2O_5	0.02	0.02	0.02	0.02	0.01	0.01	0.01	0.01	0.01	0.01	0.01
L.O.I.	0.80	1.16	1.45	0.80	1.48	0.80	0.92	0.30	0.70	0.60	1.10
Total	100.51	100.25	99.34	100.14	99.62	99.53	99.55	98.56	99.51	99.97	100.27
$Mg\#_{WR}$	0.913	0.916	0.916	0.897	0.913	0.915	0.915	0.907	0.916	0.917	0.916
$Mg\#_{ol}$	0.906	0.909	0.913	0.910	0.910	0.913	0.914	0.912	0.912	0.914	0.913
$Cr\#_{sp}$	0.302	0.356	0.362	0.365	0.371	0.392	0.392	0.394	0.399	0.394	0.399
$Mg\#_{sp}$	0.687	0.674	0.644	0.660	0.673	0.647	0.650	0.636	0.647	0.636	0.667
F (extent of melting) (%)[a]	12.04	13.68	13.84	13.89	14.09	14.62	14.57	14.69	14.82	14.68	14.82

Rock types are: Lherzolite (Lhz.), Harzburgite (Hzb.) and Dunite. Mineral abbreviations are conventional; WR: whole rock; ol: olivine; sp: spinel.

[a] From Hellebrand et al. (2001).

rectangular and triangular cross sections. Mineral grain boundaries vary from straight to gently curved, and commonly form 120° triple junctions. Mineral grains in some samples are typically fractured and show dark alteration along grain boundaries and fractures. The size of xenoliths is 1–30 cm in the longest dimensions. The boundary with the host lava is very sharp in hand specimen. The chemical modification of xenoliths by the reaction with host magma is confined only to the outer rims of xenoliths, less than 1 mm.

The xenoliths are dominantly spinel-harzburgites and dunites with minor spinel-lherzolites. They display a remarkably variable degree of fertility with a range of MgO from 36 to 48 wt.% (Table 1; Fig. 2). Although there are some samples with fertile average major element compositions, i.e. rich in basaltic components with CaO ∼3%, Al_2O_3 ∼4%, MgO <40%, the majority of the xenoliths are variably depleted in basaltic components (Table 1; Fig. 2). High contents of CaO (usually >2.2%) and Al_2O_3 (usually >2.5%) characterize some of the lherzolites as fertile and are consistent with typically high modal percent clinopyroxene (Table 1). Whole rock analyses indicate that the peridotite xenoliths as a whole display a progressive trend of depletion in fusible elements such as Ti, Ca, Al and Na with increasing the MgO content of the rocks. This depletion trend is accompanied by a decrease of the modal abundances of clinopyroxene and increase of those of olivine suggesting that the peridotites represent mantle residues from a variable extent of melt extraction (Fig. 2). Some of the xenoliths (dunites in particular), however, despite their depleted major element chemistry, contain modal olivine that is significantly higher than that would be expected for residues of small to moderate degree mantle melting. We interpret these samples as representing parts of the mantle influenced by melt/solid reactions that preferentially dissolved pyroxenes and precipitated olivine, i.e. a mineralogic reaction defined as *melt + lherzolite → melt + dunite* (e.g. Kelemen et al., 1992).

Modal proportions of major phases in mantle xenoliths were determined by point counting in thin sections and these modes are fine-tuned by geochemical mass balance using major elements (e.g. least squares mixing of mineral proportions; Table 1). The calculations were performed using the MINSQ program of Hermann and Berry (2002). All whole rock analyses used in the calculation were summed to 100% anhydrous and all Fe is reported as FeO. The typical mineral assemblage in peridotite xenoliths, as shown in Table 1, is olivine (58 to >95 vol.%, 2–4 mm), orthopyroxene (2–27%, 2–6 mm), clinopyroxene (2–13%, 2 mm) and spinel (∼2%, 1 mm). No garnetiferous xenoliths have been found in the region. However, the occurrences of some clusters can be interpreted as resulting from either decompression inducing the solid-state reaction (e.g. *garnet + olivine → orthopyroxene + clinopyroxene + spinel*) (Reid and Dawson, 1972; Smith, 1977; Henjes-Kunst and Altherr, 1992) or melting of garnet and subsequent crystallization from magma pockets (Nicolas et al., 1987). Both interpretations may imply former stability of garnet and decompression caused by vertical mass transfer near the asthenosphere–lithosphere boundary. All ultramafic xenoliths presented in this study are dry peridotites.

Some rare porphyroclastic types have been observed with textural characteristics of olivine and orthopyroxene porphyroclasts displaying moderate deformation features such as tabular sub-grains, bent exsolution lamella and curvilinear grain boundaries. Most of the xenoliths, however, are typically medium- to coarse-grained rocks with protogranular or mosaic equigranular texture and are similar to those commonly observed in worldwide spinel-peridotites (Mercier and Nicolas, 1975). Irregularly shaped spinel grains commonly intergrown with orthopyroxene characterize the samples with protogranular textures. No spinel-clinopyroxene symplectite is observed and there is no preferential association of spinel and clinopyroxene. Triple-point grain junctions are common. Some olivines in dunites show resorbed grain boundaries reflecting partial consumption of this mineral during reactions. Although no penetrative fab-

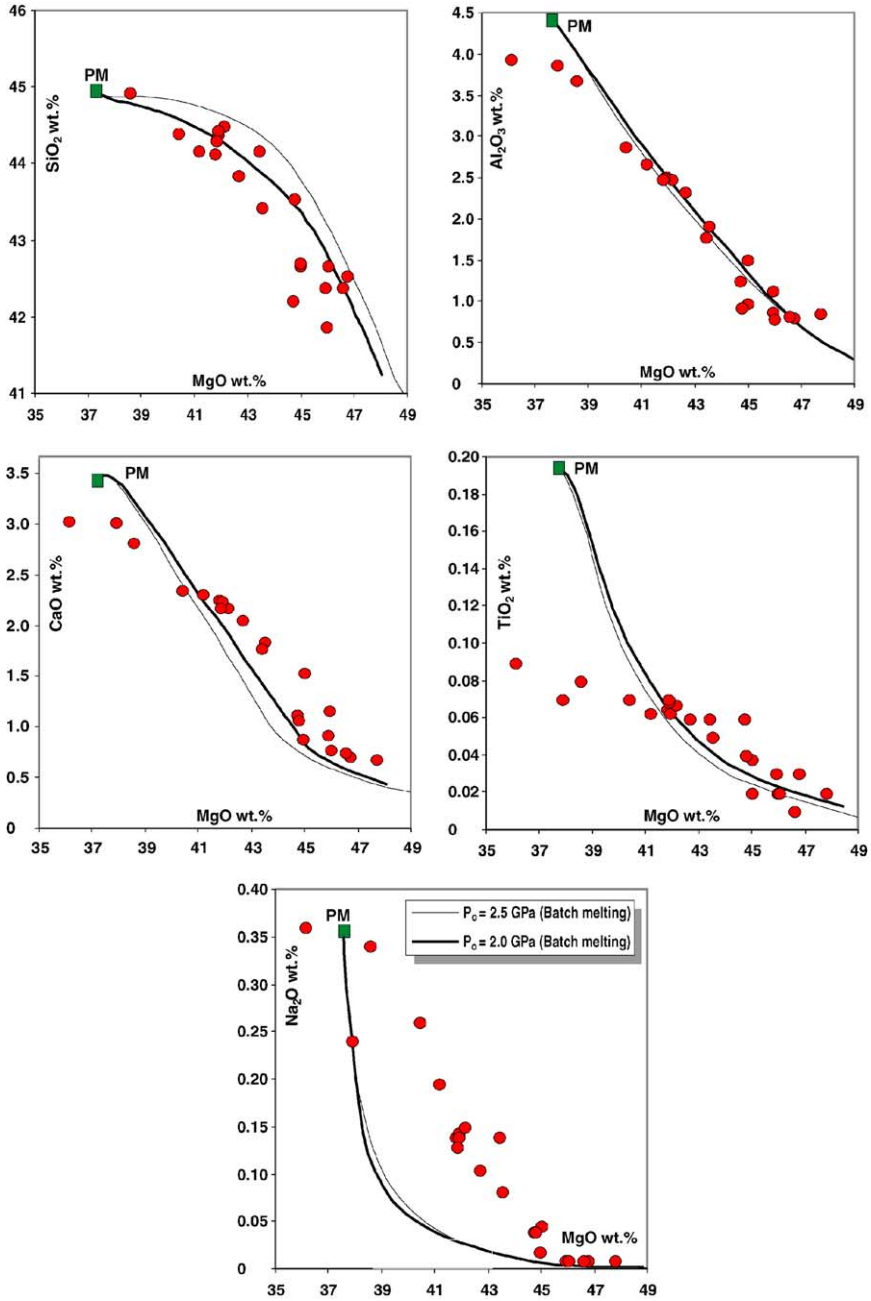

Fig. 2. Plots of SiO_2, Al_2O_3, CaO, TiO_2 and Na_2O against MgO for xenoliths from the alkaline volcanic suites of NW Turkey. The curves (or lines) represent the residues of incrementally isentropic polybaric batch melting calculated using the MELTS program. Calculations use the primitive mantle composition of McDonough and Sun (1995) as a starting source and the method described in Asimow et al. (1997). During the calculation, all liquids have been extracted from the system each time an increment of 0.5% by volume is generated by isentropic upwelling. Solid and dashed curves (or lines) correspond to melting pressures of 2.0 and 2.5 GPa, respectively.

rics (foliations or lineations) indicative of shearing or other ductile deformation have been observed in any of these protogranular xenoliths, deformation features such as sub-grain boundaries in olivine and orthopyroxene are common. These features can be regarded as reflections of either thermal shock resulted from incorporation of xenoliths into hotter basaltic melt or solid-state deformation in the mantle where they were formed (e.g. Tracy, 1980).

5. Mineral chemistry

5.1. Peridotite xenoliths

Mineral analyses of peridotites, unless otherwise stated, represent average mineral compositions within each polished thin section. The mineral compositions of spinel-peridotites from NW Turkey are typical of mantle phases, and there are no significant differences between xenoliths throughout the lava sequences. The mineral chemistry data for the peridotites are listed in Tables 2–5 .

Olivine has a very restricted compositional range of Mg# [=molar Mg/(Mg + Fe)] from 0.896 to 0.914. The range of Mg#, as well as NiO (0.24–0.42 wt.%) and MnO (0.09–0.18 wt.%), is similar to those of olivines from mantle-derived peridotite xenoliths worldwide (e.g. Frey and Prinz, 1978; Xu et al., 1996, 1998; Ionov et al., 1998). Olivines in harzburgites have higher Mg# than in lherzolites, consistent with a higher degree of melt depletion of harzburgites. The CaO contents are relatively constant for most of the samples within the range of 0.022–0.062 wt.% in harzburgite and lherzolite and 0.024–0.092 wt.% in dunite, but may reach up to 0.161 wt.%.

Orthopyroxene is an enstatite with a compositional range of $Wo_{0.5–2.3}En_{88.4–90.9}Fs_{8.3–10.2}$. The Mg# vary from 0.897 to 0.915, which are similar to or slightly, but constantly, higher than those of coexisting olivines, implying that the Fe–Mg distribution between the two phases reflects complete chemical equilibrium (Fig. 3a). Orthopyroxenes in dunites have higher Mg# and SiO_2 content, and lower Al_2O_3, TiO_2 and Na_2O than in harzburgites and lherzolites. The Cr_2O_3 contents increase from 0.15 to 0.76 wt.% with increasing the refractory nature of the rocks (Table 3). Both TiO_2 and Al_2O_3 decrease from 0.11 to 0.01 wt.% and from 4.38 to 1.79 wt.%, respectively, with increasing the Mg# of orthopyroxene.

Clinopyroxene is a diopsite with a range of $Wo_{41.3–48.3}En_{47.3–53.3}Fs_{4.4–5.4}$. The Mg# vary from 0.900 to 0.916 and display a well-defined correlation with those of olivines (Fig. 3b). The Cr_2O_3 contents increase significantly from 0.21 to 1.47 wt.% with increasing Mg#. The clinopyroxenes in most of the lherzolite and harzburgite xenoliths are characterized by increasing TiO_2, Na_2O, and decreasing CaO with increasing Al_2O_3. TiO_2 and Al_2O_3 of clinopyroxenes in most of the xenoliths decrease from 0.52 to 0.02 wt.% and from 6.96 to 2.28 wt.%, respectively, but are not correlated with Mg# (Table 4). Non-systematic variation of Na_2O and TiO_2 contents of clinopyroxenes with melt depletion indices such as clinopyroxene Mg# and whole-rock Cr# indicates that some of the compositional features, including the distribution of minor elements, for some of the samples cannot be explained solely by simple partial melting. However, Cr# [=molar Cr/(Cr + Al)] of clinopyroxene increases with that in coexisting spinel, which is an index of the degree of partial melting of the protoliths of the present xenoliths (e.g. Dick and Bullen, 1984). The range in this ratio (Fig. 4a) suggests that the spinel peridotite xenoliths from NW Turkey have experienced moderate to low degrees of partial melting. Most of the clinopyroxenes have remarkably homogeneous intra-grain compositions. The relative proportions of tetrahedral Al and octahedral Al in clinopyroxene are sensitive to the pressure and temperature of equilibration. According to the discrimination diagram of

Table 2
Average microprobe analyses of olivines in peridotite xenoliths from NW Turkey

Sample	XE7A	XE2	XE2C	XE2B	XE7B	XE1B	XE11	XE1A	XE14	XE2A	XE13A	XE10
SiO_2	40.96	40.55	40.15	40.50	40.97	41.21	40.80	40.64	40.45	40.46	40.28	40.37
TiO_2	0.01	0.00	0.00	0.00	0.01	0.00	0.00	0.03	0.03	0.00	0.02	0.00
Al_2O_3	0.00	0.00	0.01	0.00	0.02	0.00	0.01	0.00	0.00	0.00	0.02	0.00
Cr_2O_3	0.05	0.00	0.00	0.00	0.05	0.01	0.00	0.00	0.00	0.00	0.02	0.00
FeO	9.98	10.08	10.07	9.86	9.43	9.56	9.47	9.35	9.40	9.31	8.82	9.33
MnO	0.16	0.15	0.18	0.11	0.17	0.13	0.16	0.13	0.14	0.15	0.14	0.15
MgO	48.13	49.47	49.78	49.14	48.54	50.14	49.36	49.85	49.90	49.99	49.14	50.37
CaO	0.047	0.022	0.068	0.044	0.053	0.054	0.056	0.038	0.081	0.032	0.121	0.161
NiO	0.33	0.32	0.31	0.27	0.34	0.29	0.35	0.29	0.27	0.30	0.28	0.29
Total	99.67	100.64	99.96	99.96	99.58	101.36	100.21	100.30	100.26	100.26	98.85	100.67
Oxyg	4	4	4	4	4	4	4	4	4	4	4	4
Si	1.008	0.991	0.983	0.995	1.007	0.996	0.998	0.992	0.989	0.989	0.996	0.984
Ti	0.000	0.000	0.000	0.000	0.000	0.000	0.000	0.000	0.000	0.000	0.000	0.000
Al	0.000	0.000	0.000	0.000	0.001	0.000	0.000	0.000	0.000	0.000	0.001	0.000
Cr	0.001	0.000	0.000	0.000	0.001	0.000	0.000	0.000	0.000	0.000	0.000	0.000
Fe	0.205	0.206	0.206	0.202	0.194	0.193	0.194	0.191	0.192	0.190	0.182	0.190
Mn	0.003	0.003	0.004	0.002	0.004	0.003	0.003	0.003	0.003	0.003	0.003	0.003
Mg	1.766	1.802	1.817	1.799	1.778	1.806	1.799	1.814	1.819	1.822	1.811	1.830
Ca	0.001	0.001	0.002	0.001	0.001	0.001	0.001	0.001	0.002	0.001	0.003	0.004
Ni	0.007	0.006	0.006	0.005	0.007	0.006	0.007	0.006	0.005	0.006	0.006	0.006
Total	2.99	3.01	3.02	3.01	2.99	3.00	3.00	3.01	3.01	3.01	3.00	3.01
Fo	0.896	0.897	0.898	0.899	0.902	0.903	0.903	0.905	0.904	0.905	0.909	0.906

Table 2 (*Continued*)

Sample	XE13	XE13B	XE8	XE5	XE4	XE3	XE1	XE6	XE7	XE6A	XE6B
SiO_2	40.68	41.12	40.62	41.12	40.64	41.32	40.91	40.96	40.75	41.39	40.92
TiO_2	0.02	0.03	0.00	0.03	0.07	0.02	0.03	0.00	0.07	0.01	0.03
Al_2O_3	0.03	0.02	0.00	0.02	0.03	0.01	0.00	0.00	0.00	0.00	0.00
Cr_2O_3	0.03	0.03	0.00	0.03	0.05	0.00	0.00	0.00	0.01	0.01	0.03
FeO	9.12	8.91	8.65	8.91	8.87	8.68	8.57	8.69	8.78	8.39	8.67
MnO	0.11	0.16	0.11	0.16	0.17	0.13	0.13	0.09	0.13	0.13	0.13
MgO	49.54	49.76	50.66	50.86	50.36	50.85	50.83	50.75	50.77	49.78	50.97
CaO	0.140	0.077	0.031	0.029	0.016	0.033	0.029	0.017	0.024	0.073	0.092
NiO	0.24	0.33	0.32	0.33	0.33	0.28	0.31	0.30	0.32	0.42	0.35
Total	99.91	100.43	100.40	101.51	100.55	101.33	100.77	100.80	100.84	100.20	100.77
Oxyg	4	4	4	4	4	4	4	4	4	4	4
Si	0.996	1.000	0.988	0.990	0.989	0.995	0.991	0.992	0.988	1.006	0.988
Ti	0.000	0.000	0.000	0.000	0.001	0.000	0.000	0.000	0.001	0.000	0.000
Al	0.001	0.001	0.000	0.001	0.001	0.000	0.000	0.000	0.000	0.000	0.000
Cr	0.001	0.000	0.000	0.000	0.001	0.000	0.000	0.000	0.000	0.000	0.001
Fe	0.187	0.181	0.176	0.180	0.180	0.175	0.174	0.176	0.178	0.171	0.175
Mn	0.002	0.003	0.002	0.003	0.004	0.003	0.003	0.002	0.003	0.003	0.003
Mg	1.808	1.804	1.838	1.826	1.826	1.825	1.835	1.832	1.834	1.804	1.835
Ca	0.004	0.002	0.001	0.001	0.000	0.001	0.001	0.000	0.001	0.002	0.002
Ni	0.005	0.006	0.006	0.006	0.006	0.005	0.006	0.006	0.006	0.008	0.007
Total	3.00	3.00	3.01	3.01	3.01	3.00	3.01	3.01	3.01	2.99	3.01
Fo	0.906	0.909	0.913	0.910	0.910	0.913	0.914	0.912	0.912	0.914	0.913

Table 3
Average microprobe analyses of orhopyroxenes in peridotite xenoliths from NW Turkey

Sample	XE7A	XE2	XE2C	XE2B	XE7B	XE1B	XE11	XE1A	XE14	XE2A	XE13A	XE10
SiO_2	54.26	56.06	55.05	55.55	54.83	55.59	55.13	55.46	55.13	55.72	55.54	55.57
TiO_2	0.11	0.09	0.10	0.12	0.08	0.07	0.10	0.07	0.08	0.07	0.07	0.08
Al_2O_3	4.38	3.31	3.30	3.68	4.33	3.37	4.31	3.24	4.15	2.88	4.05	4.19
Cr_2O_3	0.49	0.15	0.57	0.43	0.38	0.44	0.47	0.48	0.49	0.46	0.68	0.78
FeO	6.74	6.53	6.74	6.69	6.46	6.41	6.26	6.40	6.25	6.46	5.78	5.89
MnO	0.13	0.19	0.21	0.19	0.20	0.14	0.11	0.16	0.17	0.15	0.13	0.13
MgO	32.78	32.40	33.65	33.78	33.36	33.94	32.93	34.27	33.55	34.72	32.52	32.23
CaO	0.75	0.39	0.59	0.56	0.71	0.58	0.71	0.47	0.69	0.49	1.09	1.18
Na_2O	0.06	0.02	0.03	0.01	0.05	0.02	0.10	0.00	0.06	0.01	0.13	0.16
Total	99.70	99.13	100.24	101.01	100.40	100.54	100.12	100.09	100.57	100.96	99.99	100.21
Oxyg	6	6	6	6	6	6	6	6	6	6	6	6
Si	1.887	1.948	1.905	1.904	1.891	1.912	1.903	1.908	1.896	1.911	1.917	1.915
Ti	0.003	0.002	0.003	0.003	0.002	0.002	0.003	0.002	0.002	0.002	0.002	0.002
Al	0.180	0.136	0.134	0.149	0.176	0.137	0.175	0.131	0.168	0.116	0.165	0.170
Cr	0.013	0.004	0.016	0.012	0.010	0.012	0.013	0.013	0.013	0.012	0.019	0.021
Fe	0.196	0.190	0.195	0.192	0.186	0.184	0.181	0.184	0.180	0.185	0.167	0.170
Mn	0.004	0.006	0.006	0.005	0.006	0.004	0.003	0.005	0.005	0.004	0.004	0.004
Mg	1.700	1.679	1.736	1.727	1.715	1.740	1.694	1.758	1.720	1.774	1.673	1.656
Ca	0.028	0.014	0.022	0.021	0.026	0.021	0.026	0.017	0.025	0.018	0.040	0.044
Na	0.004	0.001	0.002	0.000	0.003	0.001	0.007	0.000	0.004	0.001	0.009	0.011
Total	4.01	3.99	4.01	4.01	4.01	4.01	4.00	4.01	4.01	4.01	3.99	3.99
Wo	1.45	0.77	1.12	1.06	1.36	1.10	1.38	0.88	1.32	0.91	2.14	2.33
En	88.36	89.15	88.90	89.05	88.97	89.43	89.12	89.73	89.34	89.72	88.98	88.59
Fs	10.19	10.08	9.98	9.89	9.67	9.48	9.50	9.39	9.34	9.37	8.87	9.08
Mg#	0.897	0.898	0.899	0.900	0.902	0.904	0.904	0.905	0.905	0.905	0.909	0.907

Table 3 (*Continued*)

Sample	XE13	XE13B	XE8	XE5	XE4	XE3	XE1	XE6	XE7	XE6A	XE6B
SiO_2	55.04	55.84	56.13	56.84	56.64	56.66	56.23	57.04	56.79	55.96	56.02
TiO_2	0.08	0.06	0.05	0.04	0.04	0.04	0.02	0.01	0.03	0.04	0.04
Al_2O_3	4.06	2.77	2.70	2.00	2.05	2.22	2.23	1.79	1.84	3.18	3.05
Cr_2O_3	0.79	0.71	0.29	0.37	0.27	0.54	0.53	0.37	0.35	0.49	0.76
FeO	5.86	5.91	5.87	5.74	5.84	5.98	5.83	5.88	6.00	5.47	5.49
MnO	0.13	0.13	0.12	0.16	0.15	0.17	0.10	0.15	0.13	0.13	0.14
MgO	32.09	33.25	34.56	33.32	33.54	35.07	35.09	35.16	35.22	33.21	33.15
CaO	1.14	0.88	0.38	0.49	0.40	0.51	0.48	0.29	0.35	0.72	0.97
Na_2O	0.13	0.04	0.00	0.00	0.02	0.02	0.02	0.01	0.02	0.06	0.08
Total	99.32	99.59	100.46	98.97	100.68	100.20	100.61	100.68	100.68	99.26	99.70
Oxyg	6	6	6	6	6	6	6	6	6	6	6
Si	1.914	1.935	1.931	1.973	1.967	1.932	1.929	1.950	1.944	1.938	1.936
Ti	0.002	0.002	0.001	0.001	0.001	0.001	0.001	0.000	0.001	0.001	0.001
Al	0.166	0.113	0.109	0.082	0.084	0.089	0.090	0.072	0.074	0.130	0.124
Cr	0.022	0.019	0.008	0.010	0.007	0.015	0.014	0.010	0.009	0.013	0.021
Fe	0.170	0.171	0.169	0.167	0.169	0.171	0.167	0.168	0.172	0.158	0.159
Mn	0.004	0.004	0.004	0.005	0.004	0.005	0.003	0.004	0.004	0.004	0.004
Mg	1.664	1.718	1.773	1.724	1.736	1.783	1.795	1.792	1.797	1.715	1.708
Ca	0.042	0.033	0.014	0.018	0.015	0.019	0.018	0.011	0.013	0.027	0.036
Na	0.009	0.003	0.000	0.000	0.002	0.001	0.001	0.001	0.001	0.004	0.005
Total	3.99	4.00	4.01	3.99	3.99	4.01	4.01	4.01	4.01	3.99	3.99
Wo	2.26	1.70	0.72	0.95	0.78	0.94	0.90	0.54	0.64	1.41	1.89
En	88.65	89.39	90.64	90.32	90.39	90.41	90.65	90.93	90.69	90.25	89.77
Fs	9.08	8.91	8.64	8.72	8.82	8.65	8.46	8.54	8.66	8.34	8.34
Mg#	0.907	0.909	0.913	0.912	0.911	0.913	0.915	0.914	0.913	0.915	0.915

Table 4
Average microprobe analyses of clinopyroxenes in peridotite xenoliths from NW Turkey

Sample	XE7A	XE2	XE2C	XE2B	XE7B	XE1B	XE11	XE1A	XE14	XE2A
SiO_2	51.82	52.50	53.54	52.01	52.22	51.87	51.85	50.78	52.13	51.07
TiO_2	0.36	0.03	0.04	0.49	0.35	0.44	0.43	0.52	0.40	0.50
Al_2O_3	5.63	3.40	2.62	6.41	5.10	6.52	6.48	6.83	5.82	6.94
Cr_2O_3	0.43	0.31	0.21	0.51	0.63	0.75	0.98	0.82	0.82	0.78
FeO	3.19	3.13	3.15	2.95	2.98	2.81	2.77	2.87	2.81	2.80
MnO	0.07	0.06	0.09	0.08	0.09	0.07	0.05	0.12	0.06	0.09
MgO	16.11	16.45	17.01	15.60	16.09	15.36	15.29	16.08	16.08	15.67
CaO	20.88	22.37	22.08	20.29	21.19	19.98	20.33	20.44	20.45	20.25
Na_2O	1.00	0.64	0.44	1.71	0.97	1.77	1.50	1.76	1.20	1.79
Total	99.49	98.89	99.18	100.05	99.62	99.57	99.68	100.22	99.77	99.89
Oxyg	6	6	6	6	6	6	6	6	6	6
Si	1.887	1.930	1.957	1.881	1.900	1.883	1.881	1.841	1.889	1.854
Ti	0.010	0.001	0.001	0.013	0.010	0.012	0.012	0.014	0.011	0.014
Al	0.242	0.147	0.113	0.273	0.219	0.279	0.277	0.292	0.249	0.297
Cr	0.012	0.009	0.006	0.015	0.018	0.022	0.028	0.024	0.023	0.022
Fe	0.097	0.096	0.096	0.089	0.091	0.085	0.084	0.087	0.085	0.085
Mn	0.002	0.002	0.003	0.002	0.003	0.002	0.002	0.004	0.002	0.003
Mg	0.875	0.902	0.927	0.841	0.873	0.831	0.827	0.869	0.869	0.848
Ca	0.815	0.881	0.865	0.786	0.826	0.777	0.790	0.794	0.794	0.788
Na	0.071	0.046	0.031	0.120	0.068	0.125	0.106	0.124	0.084	0.126
Total	4.01	4.01	4.00	4.01	4.01	4.01	4.01	4.01	4.01	4.01
Wo	45.60	46.90	45.80	45.80	46.16	45.88	46.45	45.37	45.43	45.77
En	48.96	47.98	49.10	49.00	48.77	49.08	48.61	49.66	49.70	49.29
Fs	5.44	5.12	5.10	5.20	5.07	5.04	4.94	4.97	4.87	4.94
Mg#	0.900	0.904	0.906	0.904	0.906	0.907	0.908	0.909	0.911	0.909

Table 4 (*Continued*)

Sample	XE13A	XE10	XE13	XE13B	XE8	XE5	XE4	XE3	XE1	XE6
SiO_2	52.25	51.83	52.38	52.93	50.08	53.52	52.38	53.13	52.50	51.74
TiO_2	0.27	0.51	0.24	0.05	0.52	0.05	0.06	0.02	0.02	0.02
Al_2O_3	5.79	6.69	5.28	3.13	6.96	2.56	2.28	2.49	3.40	2.89
Cr_2O_3	1.14	1.09	1.19	1.15	1.13	1.20	1.15	1.11	1.14	1.29
FeO	2.89	3.12	2.97	2.99	2.78	2.88	2.92	2.64	2.83	2.93
MnO	0.09	0.10	0.08	0.08	0.07	0.08	0.07	0.11	0.07	0.05
MgO	16.41	17.30	16.62	17.02	16.01	17.01	16.82	15.81	16.74	17.54
CaO	19.40	18.62	19.16	21.11	20.91	22.81	22.70	22.46	22.38	23.36
Na_2O	1.31	1.42	1.30	0.61	1.68	0.25	0.39	0.32	0.63	0.42
Total	99.55	100.68	99.22	99.07	100.14	100.36	98.76	98.09	99.71	100.24
Oxyg	6	6	6	6	6	6	6	6	6	6
Si	1.894	1.858	1.905	1.937	1.823	1.939	1.934	1.965	1.916	1.904
Ti	0.007	0.014	0.007	0.001	0.014	0.001	0.002	0.001	0.001	0.001
Al	0.247	0.283	0.226	0.135	0.299	0.109	0.099	0.109	0.146	0.123
Cr	0.033	0.031	0.034	0.033	0.033	0.034	0.034	0.032	0.033	0.037
Fe	0.088	0.094	0.090	0.091	0.085	0.087	0.090	0.082	0.086	0.088
Mn	0.003	0.003	0.002	0.002	0.002	0.002	0.002	0.003	0.002	0.002
Mg	0.887	0.925	0.901	0.928	0.869	0.919	0.926	0.872	0.911	0.944
Ca	0.754	0.715	0.747	0.828	0.815	0.886	0.898	0.890	0.875	0.903
Na	0.092	0.099	0.092	0.043	0.119	0.018	0.028	0.023	0.045	0.029
Total	4.00	4.01	4.00	4.00	4.01	4.00	4.01	3.99	4.01	4.01
Wo	43.61	41.26	42.96	44.80	46.10	46.81	46.92	48.28	46.74	46.67
En	51.32	53.34	51.85	50.25	49.11	48.57	48.37	47.29	48.65	48.76
Fs	5.07	5.40	5.20	4.95	4.78	4.61	4.71	4.43	4.61	4.57
Mg#	0.910	0.908	0.909	0.910	0.911	0.913	0.911	0.914	0.913	0.914

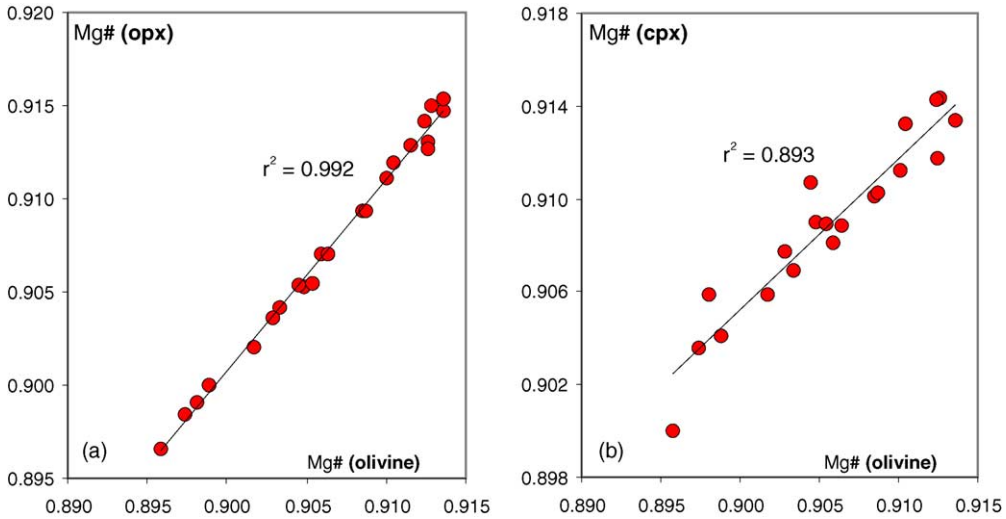

Fig. 3. (a and b) The relationship between Mg# of olivine and pyroxenes of the peridotite xenoliths from NW Turkey display well-defined correlation.

Seyler and Bonatti (1994), all peridotite xenoliths from NW Turkey lie in the field of continental xenoliths (Fig. 4b).

Spinels display a remarkably large variation in spinel Cr# that range from 0.126 to 0.399 (Table 1). Although some spinels in lherzolite and harzburgite samples are aluminous with Cr# <0.250 and largely display a moderately fertile character, most samples are significantly depleted with Cr# of 0.350 to 0.399. A great number of samples show no significant within-sample variation, as they are compositionally homogeneous on a thin section scale. The low TiO_2 concentrations in the spinels of the xenoliths attest to the residual nature of the samples. The Mg# of spinels range from 0.636 to 0.783, which are lower than any silicate minerals. Spinels in dunites have lower Al_2O_3 and MgO, and higher Cr_2O_3 and FeO contents than in harzburgites and lherzolites (Table 5).

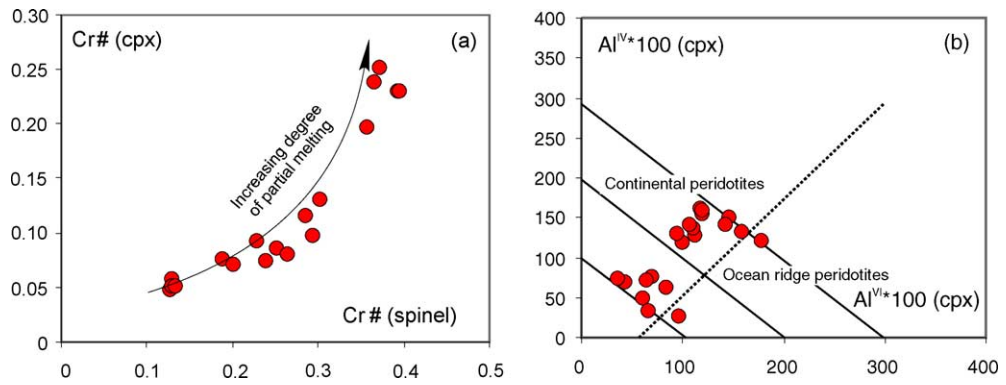

Fig. 4. (a) The relationship between Cr/(Cr + Al) ratio in clinopyroxene and spinel. (b) Tetrahedral Al and octahedral Al in clinopyroxene from the peridotite xenoliths of NW Turkey plotted on the Seyler and Bonatti (1994) diagram discriminating pyroxene compositions from continental and oceanic peridotites.

Table 5
Average microprobe analyses of spinels in peridotite xenoliths from NW Turkey

Sample	XE7A	XE2	XE2C	XE2B	XE7B	XE1B	XE11	XE1A	XE14	XE2A	XE13A	XE10
SiO_2	0.04	0.00	0.05	0.06	0.04	0.04	0.04	0.03	0.06	0.03	0.01	0.02
TiO_2	0.14	0.14	0.16	0.15	0.06	0.02	0.11	0.05	0.17	0.13	0.15	0.27
Al_2O_3	54.26	53.48	53.81	52.95	49.10	47.63	46.77	44.38	43.19	42.48	42.70	41.43
Cr_2O_3	11.66	11.67	11.95	12.14	17.02	17.69	20.51	20.69	21.65	22.64	25.23	25.55
FeO	12.64	13.33	13.31	13.54	14.98	14.70	14.90	15.77	15.70	15.66	15.16	15.82
MnO	0.13	0.16	0.07	0.17	0.00	0.14	0.12	0.12	0.21	0.12	0.06	0.07
MgO	20.51	19.51	19.40	19.59	18.66	18.41	18.35	17.48	17.60	17.83	15.58	16.36
Total	99.38	98.63	99.07	98.92	99.86	98.92	100.80	98.74	98.57	99.16	98.89	99.52
Oxyg	4	4	4	4	4	4	4	4	4	4	4	4
Si	0.001	0.000	0.001	0.002	0.001	0.001	0.001	0.001	0.002	0.001	0.000	0.001
Ti	0.003	0.003	0.003	0.003	0.001	0.000	0.002	0.001	0.004	0.003	0.003	0.006
Al	1.691	1.692	1.694	1.675	1.569	1.547	1.498	1.469	1.434	1.411	1.422	1.379
Cr	0.244	0.248	0.252	0.258	0.365	0.385	0.441	0.459	0.482	0.504	0.563	0.570
Fe	0.279	0.299	0.297	0.304	0.340	0.339	0.339	0.370	0.370	0.369	0.358	0.374
Mn	0.003	0.004	0.001	0.004	0.000	0.003	0.003	0.003	0.005	0.003	0.001	0.002
Mg	0.808	0.781	0.773	0.784	0.754	0.756	0.744	0.731	0.739	0.749	0.656	0.689
Total	3.01	3.01	3.01	3.01	3.01	3.01	3.01	3.01	3.01	3.01	3.00	3.02

Table 5 (*Continued*)

Sample	XE13	XE13B	XE8	XE5	XE4	XE3	XE1	XE6	XE7	XE6A	XE6B
SiO_2	0.01	0.01	0.04	0.04	0.01	0.01	0.01	0.01	0.03	0.01	0.01
TiO_2	0.21	0.08	0.11	0.13	0.04	0.05	0.05	0.05	0.05	0.05	0.13
Al_2O_3	41.09	35.85	34.56	34.81	34.51	33.06	32.90	32.90	32.36	32.86	34.06
Cr_2O_3	26.56	29.59	29.19	29.87	30.37	31.72	31.64	31.93	32.05	31.79	33.74
FeO	15.53	17.12	18.59	18.29	17.51	18.45	18.31	18.91	18.64	18.92	15.97
MnO	0.06	0.08	0.10	0.12	0.16	0.16	0.23	0.16	0.18	0.16	0.07
MgO	15.33	15.89	15.07	15.92	16.20	15.21	15.29	14.81	15.32	14.82	14.33
Total	98.79	98.62	97.88	99.39	99.04	98.84	98.61	98.92	98.83	98.61	98.31
Oxyg	4	4	4	4	4	4	4	4	4	4	4
Si	0.000	0.000	0.001	0.001	0.000	0.000	0.000	0.000	0.001	0.000	0.000
Ti	0.005	0.002	0.002	0.003	0.001	0.001	0.001	0.001	0.001	0.001	0.003
Al	1.380	1.236	1.215	1.203	1.196	1.160	1.157	1.156	1.139	1.157	1.187
Cr	0.598	0.685	0.689	0.693	0.706	0.746	0.746	0.753	0.757	0.751	0.789
Fe	0.370	0.419	0.464	0.449	0.431	0.459	0.457	0.471	0.465	0.473	0.395
Mn	0.001	0.002	0.003	0.003	0.004	0.004	0.006	0.004	0.005	0.004	0.002
Mg	0.651	0.693	0.670	0.696	0.710	0.675	0.680	0.658	0.682	0.660	0.632
Total	3.01	3.01	3.01	3.01	3.01	3.01	3.01	3.01	3.01	3.01	3.01

As a whole, there are consistent compositional correlations between constituent phases in the lherzolite and harzburgite xenoliths. Mg/(Mg + Fe) ratios are broadly correlated between the constituent phases with Mg# successively lower from clinopyroxene through orthopyroxene, olivine to spinel. Calculated Fe–Mg partition coefficients between coexisting silicate mineral pairs for the xenoliths lie within narrow ranges (e.g. $K_D^{ol\text{-}opx} = 1.00–1.02$), indicating equilibration has been attained. Cr/(Cr + Al) ratios in spinel show positive correlations with those in coexisting clinopyroxene and orthopyroxene and with Fo in olivine.

The composition of residual phases in peridotites changes continuously during partial melting. For example, Fe contents of silicate minerals, and Al contents of spinel decrease with increasing degree of partial melting, whereas Mg of silicate minerals and Cr of spinel generally increase. Therefore, the Mg/Fe ratios (or Mg#) of silicate minerals, and Cr/Al ratios (or Cr#) of spinel could be used as an indicator of the degree of partial melting (e.g. Song and Frey, 1989; Dick and Bullen, 1984; Hellebrand et al., 2001). The Mg# between pyroxenes and olivines in peridotites of NW Turkey have distinct positive correlations (Fig. 3a and b), indicating residual character of these rocks after various degree of partial melting. Harzburgites have higher Cr# of spinel and Mg# of silicates, and lower Mg# of spinel than lherzolites. This suggests that least depleted lherzolites represent relatively primitive mantle that has undergone only a small degree of partial melting. However, harzburgites represent residual mantle following larger degrees of partial melting compared with lherzolites.

Variations in mineral compositions between the peridotite samples are perhaps best illustrated on the plot of the Cr# in spinel against the forsterite content of coexisting olivine (Fig. 5a), where all samples plot within, or close to, the olivine-spinel mantle array (or residual peridotite array) defined by Arai (1992), and are characterized by ∼3 to ∼15% melting of a source close to the primitive mantle compositions. Linear variation of the spinel Cr# and forsterite content of olivine in Fig. 5a is consistent with the residual origin of the peridotites, indicating that none of the xenoliths presented in this study is of cumulate origin, for which a marked displacement from the olivine-spinel mantle array towards lower olivine forsterite contents would be required (e.g. Arai, 1992). The plot of spinel Cr# against spinel Mg# in Fig. 5b further indicates that the spinel compositions from the xenoliths of NW Turkey have fairly narrow compositional ranges resembling those from abyssal peridotites.

5.2. Alkaline lavas

Rare *olivines* (<5%) in some alkali basalts and basanites have a mosaic texture and incipient undulose extinction. These unhedral crystals have broken or ragged outlines and may be overgrown with a fringe of small olivine crystals. They mostly display reverse compositional zoning and certainly represent entrained material from desintagrated peridotite xenoliths and were not considered in the present study. The dominant olivine phenocrysts within the alkaline lavas are commonly euhedral and subhedral minerals, 2–4 mm in diameter with sharply defined crystal edges. Their abundances range between 40 and 70% of the total phenocrysts. In some samples, olivines are more skeletal with evidence of marginal resorptions, rapid cooling and internal cavities. Their grain size in these samples is usually less than 3 mm. Rare inclusions of spinels have been observed in both types of olivine phenocrysts. No significant systematic compositional zoning has been observed in the olivine phenocrysts; core and rim compositions are $Fo_{83–92}$ and $Fo_{81–91}$, respectively. NiO and CaO contents of olivines range from 0.10 to 0.33 wt.% and from 0.21 to 0.30 wt.%, respectively (Table 6).

Exchange coefficients (K_D values) calculated for the distribution of Fe and Mg between olivine phenocrysts and liquids similar in composition of host whole-rocks $[(X_{FeO}/X_{MgO})_{ol}/(X_{FeO}/X_{MgO})_{liq}]$ (X is the

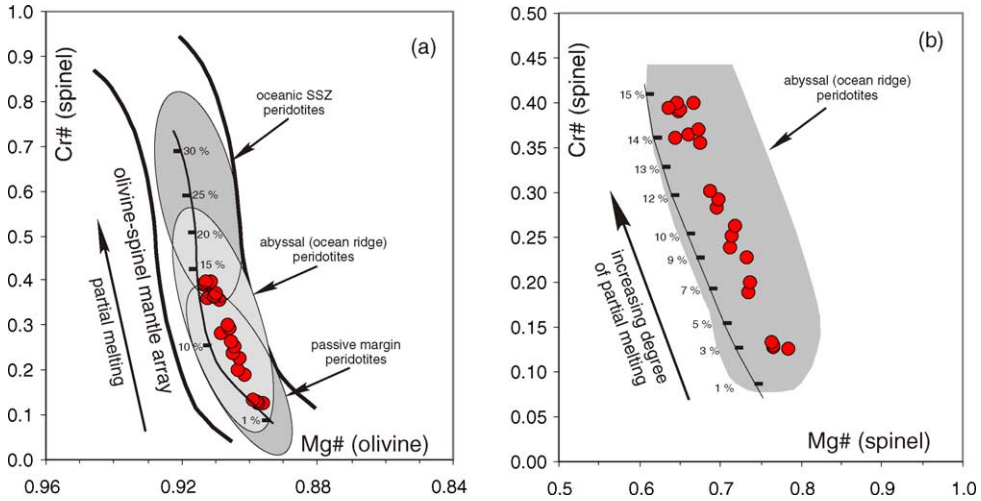

Fig. 5. (a) Plot of spinel Cr# against olivine Mg# for the ultramafic peridotite xenoliths from NW Turkey. Also plotted for comparison are the fields of abyssal (ocean ridge) peridotites (Dick and Bullen, 1984), the oceanic supra-subduction zone peridotites and passive continental margin peridotites (Pearce et al., 1999), the olivine spinel mantle array and melting trend (Arai, 1992). The plot shows that the xenoliths have spinel and olivine compositions resembling to those from abyssal peridotites and passive margin peridotites. (b) Plot of spinel Cr# against spinel Mg# for the peridotite xenoliths. Spinel compositions from abyssal peridotites (Dick and Bullen, 1984) are shown for comparison to illustrate the fairly narrow compositional range of plagioclase- and garnet-free peridotites. Also plotted the model partial melting trajectory for peridotite (the solid line) obtained from the calculating the average degree of melting for each sample using the numerical expression of Hellebrand et al., (2001). Thick marks on the line correspond to degrees of partial melting after which each peridotite xenolith has been remained as a mantle residual.

mole fraction) range between 0.24 and 0.31 for the alkaline basalt and basanites. Using the experimental results of Roeder and Emslie (1970), the Mg/Fe ratios of the liquid with which the olivine composition would have been in equilibrium can be calculated and compared with the Mg/Fe of the bulk rock, to assess whether the olivines are in equilibrium with their host lavas. The result of such calculation is shown in Fig. 6a, where most of the olivine phenocrysts from the alkaline lavas of NW Turkey are shown to be within the equilibrium range with few exceptions that are only slightly out of the equilibrium range.

Clinopyroxene phenocrysts generally display glomerophyric textures, forming spherulite shapes with clustered clinopyroxene crystals radiating outwards from early-formed olivine crystals. Almost all clinopyroxene phenocrysts and microphenocrysts characteristically have high-Ca contents ranging between $Wo_{43–49}$. Their compositions are predominantly diopsite, titan augite and titanian augite according to the I.M.A. classification (Morimonto, 1989). Chemical compositions of clinopyroxenes do not vary considerably with respect to major element chemistry of the host lavas, nor can any systematic variations be observed between core and rim composition of clinopyroxenes, although some phenocrysts display a slight (but non-systematic) core-to rim variations in X_{Mg}, Al^{VI}/Al^{IV} and Al/Ti ratios.

Plagioclase does not occur as a phenocryst phase, but some samples contain plagioclase laths in their microcrystalline groundmass. Flow alignment of groundmass plagioclase imparts a weak trachytic texture in these samples. Most of the analyzed groundmass plagioclase laths or microphenocrysts are Ca-rich with anortite contents ranging between $An_{77–95}$.

Table 6
Average microprobe analyses of olivine phenocrysts and microphenocrysts for the whole compositional range of mafic alkaline lavas from NW Turkey

Sample	EA512	EA519	EA508	EA514	EA522	EA531	EA520	EA252	EA515	EA510	EA534	EA537	EA509	EA517	EA517	EA516	EA511
SiO_2	38.71	39.34	38.42	39.12	39.24	39.06	37.21	40.14	39.61	40.14	40.25	40.37	40.19	39.54	40.44	40.65	41.12
TiO_2	0.03	0.02	0.04	0.02	0.01	0.01	0.00	0.03	0.01	0.02	0.00	0.00	0.01	0.02	0.01	0.00	0.02
Al_2O_3	0.04	0.06	0.02	0.05	0.00	0.04	0.04	0.04	0.03	0.03	0.01	0.00	0.02	0.00	0.01	0.01	0.03
Cr_2O_3	0.07	0.04	0.03	0.02	0.05	0.08	0.00	0.04	0.00	0.04	0.02	0.00	0.03	0.00	0.00	0.01	0.00
FeO	15.35	14.67	14.67	14.03	13.18	12.97	13.20	12.02	11.91	11.46	11.42	10.95	10.66	10.29	9.73	9.18	8.57
MnO	0.23	0.20	0.31	0.20	0.14	0.37	0.43	0.39	0.59	0.36	0.23	0.13	0.28	0.16	0.15	0.13	0.10
MgO	44.85	45.40	47.05	46.16	47.43	47.24	48.12	47.15	48.23	47.67	48.56	48.92	48.38	49.97	50.03	50.09	49.19
CaO	0.25	0.27	0.22	0.27	0.26	0.25	0.24	0.24	0.25	0.24	0.22	0.24	0.25	0.21	0.22	0.23	0.22
NiO	0.23	0.18	0.15	0.13	0.16	0.13	0.11	0.12	0.09	0.13	0.20	0.25	0.17	0.29	0.29	0.29	0.33
Na_2O	0.02	0.03	0.02	0.02	0.03	0.03	0.02	0.02	0.00	0.01	0.01	0.00	0.01	0.00	0.00	0.00	0.00
K_2O	0.00	0.04	0.01	0.01	0.00	0.01	0.00	0.00	0.00	0.01	0.01	0.01	0.02	0.00	0.00	0.00	0.00
Total	99.78	100.23	100.93	100.01	100.50	100.17	99.37	100.20	100.72	100.12	100.94	100.87	100.00	100.48	100.88	100.59	99.57
Oxyg	4	4	4	4	4	4	4	4	4	4	4	4	4	4	4	4	4
Si	0.980	0.994	0.960	0.994	0.976	0.987	0.942	0.994	0.983	0.993	0.987	0.988	0.991	0.980	0.985	0.990	1.007
Ti	0.001	0.000	0.001	0.000	0.000	0.000	0.000	0.001	0.000	0.000	0.000	0.000	0.000	0.000	0.000	0.000	0.000
Al	0.001	0.002	0.001	0.001	0.000	0.001	0.001	0.001	0.001	0.001	0.000	0.000	0.001	0.000	0.000	0.000	0.001
Cr	0.001	0.001	0.000	0.000	0.001	0.002	0.000	0.001	0.000	0.001	0.000	0.000	0.001	0.000	0.000	0.000	0.000
Fe	0.325	0.305	0.307	0.291	0.274	0.267	0.280	0.249	0.245	0.237	0.234	0.224	0.220	0.210	0.198	0.187	0.176
Mn	0.005	0.004	0.007	0.004	0.003	0.008	0.009	0.008	0.012	0.008	0.005	0.003	0.006	0.003	0.003	0.003	0.002
Mg	1.693	1.686	1.753	1.704	1.759	1.736	1.816	1.741	1.767	1.757	1.775	1.785	1.779	1.815	1.817	1.818	1.795
Ca	0.007	0.007	0.006	0.007	0.007	0.007	0.007	0.006	0.007	0.006	0.006	0.006	0.006	0.006	0.006	0.006	0.006
Ni	0.005	0.004	0.003	0.003	0.003	0.003	0.002	0.002	0.002	0.003	0.004	0.005	0.003	0.006	0.006	0.006	0.007
Na	0.001	0.002	0.001	0.001	0.001	0.001	0.001	0.001	0.000	0.001	0.000	0.000	0.000	0.000	0.000	0.000	0.000
K	0.000	0.001	0.000	0.000	0.000	0.000	0.000	0.000	0.000	0.000	0.000	0.000	0.000	0.000	0.000	0.000	0.000
Total	3.01	3.01	3.02	3.01	3.01	3.01	3.02	3.00	3.02	3.01	3.01	3.01	3.01	3.02	3.01	3.01	2.99
Fo	0.839	0.847	0.851	0.854	0.865	0.867	0.867	0.875	0.878	0.881	0.883	0.888	0.890	0.896	0.902	0.907	0.911

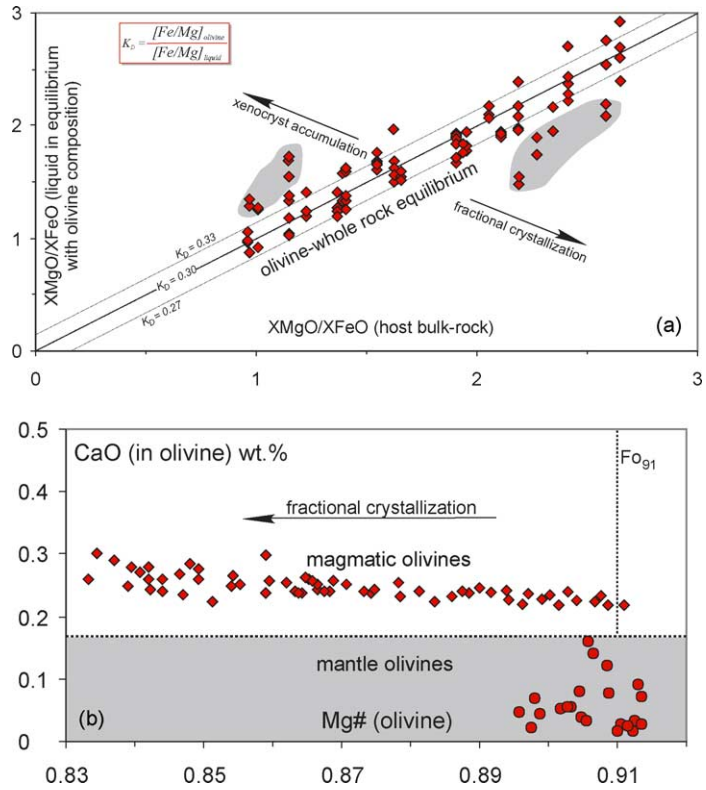

Fig. 6. (a) Equilibrium X_{MgO}/X_{FeO} ratio of liquid calculated from olivine compositions plotted against X_{MgO}/X_{FeO} ratio of host bulk-rock from the lava flows of NW Turkey. X is the mole fraction of the oxide. Lines represent equilibrium between minerals and bulk rock compositions. Equilibrium range was calculated using equilibrium $^{Fe/Mg}K_{Dmin/liq}$ values from Roeder and Emslie, (1970). The olivine compositions are generally in Mg–Fe exchange equilibrium with the primary melt compositions of the host lavas at a K_D value of 0.30. They are, therefore, thought to have formed from the melt, probably during magma transport through the lithosphere shortly before the melt extraction. A Small number of olivine phenocrysts are not in equilibrium with their host lavas and are believed to have either formed as accumulated xenocrysts or crystallized from relatively evolved magmas. (b) Affinities of the olivine phenocrysts and micro-phenocrysts (shown as closed diamonds) from the alkaline lavas of NW Turkey. The plot of olivine CaO as a function of Mg# (% forsterite) shows that the olivines crystallized from a related suite of magmas and are not disrupted xenocrysts from mantle or other sources (see text for details). For comparison, mantle olivines (from the peridotite xenoliths; shown as closed circles) analyzed simultaneously are also shown: in contrast to the igneous olivines the mantle olivines have very low CaO contents.

Oxide phases of *ilmenite* and *magnetite* are present exclusively in groundmass and in interstitial position. They form euhedral and subhedral microcrysts that range in size from ~1 to 0.05 mm. Modal proportions of the oxides range from 5 to 15% by volume of phenocrysts. Magnetite shows a wide range of composition (Ulvöspinel content from 28 to 87%), while ilmenite show much less solid solution (ilmenite content from 90 to 98%), indicating weakly oxidizing conditions of formation.

6. Temperature and pressure estimates

Some of the xenoliths from the NW Turkish alkaline suite exhibit significant intra-grain compositional variations reflecting partial re-equilibration due to changing thermal conditions characterizing the

mantle environment prior to entrainment in melts. We have, therefore, excluded these samples from the calculation, as they would give unreliable estimates of pressure and temperature. In contrast the majority of the samples are chemically homogeneous. These xenoliths were probably equilibrated under ambient pressure and temperature conditions within the upper mantle and escaped partial re-equilibration after entrainment in melt. Sharp boundary of xenoliths with host basalts demonstrates that the xenoliths were transported quickly to the surface, being captured in ascending basalt without being chemically disturbed by the host basalt significantly. The complete homogeneity of the constituent minerals is compelling evidence for complete chemical equilibration at a certain temperature. Thus, the core–core pairs of minerals should record the final temperature and pressure at which those minerals ceases exchanging elements, prior to be incorporated into host magma.

6.1. Equilibration temperatures of the xenoliths

There are numerous published geothermometers applicable to mantle assemblages of spinel-peridotite, each with their own set of limitations and none having a particular universal application or support. In this context, equilibrium temperatures of mantle phases can be calculated using geothermometers calibrated against: (1) enstatite component of coexisting two pyroxenes (Wood and Banno, 1973; Wells, 1977; Bertrand and Mercier, 1985; Brey and Köhler, 1990); (2) Al-solubility in orthopyroxene coexisting with olivine and spinel (Sachtleben and Seck, 1981; Webb and Wood, 1986); (3) the Cr–Al partitioning between orthopyroxene and spinel coexisting with olivine (Witt-Eickschein and Seck, 1991); (4) Ca component in orthopyroxene (Brey and Köhler, 1990); and (5) Mg–Fe^{2+} exchange between olivine and spinel (Ballhaus et al., 1991). To establish the temperatures of equilibration of the xenoliths from NW Turkey, two formulations of Brey and Köhler (1990) based on the pyroxene solvus were used. The first, using the distribution of the (Mg,Fe)SiO_3 component between coexisting orthopyroxene and clinopyroxene, is referred to as T_{BK}, and the second, using the Ca content of the orthopyroxene (assumed to be in equilibrium with clinopyroxene), is referred to as $T_{Ca\text{-}in\text{-}opx}$. Limitations of the thermometers are that they are dependent on the pressure of formation of the xenoliths (which has to be assumed), and the first requires knowledge of the Fe^{3+} content of the coexisting clinopyroxene, which, although likely to be very small, is not known from microprobe analyses.

Table 7 shows the temperatures obtained for the peridotite xenoliths using the above geothermometers calculated for a pressure of equilibration of 2.0 GPa. This pressure was chosen as it falls within the experimentally determined stability field for spinel-peridotites (e.g. O'Neill, 1981) and is commonly used in the literature, allowing for ease of comparison with other studies. The absence of equilibrium clinopyroxenes in some of the xenoliths (dunites in particular) negates the use of these geothermometers to estimate their temperature of equilibrations. The range in equilibrium temperatures obtained using T_{BK} is 811–1178, whereas that obtained using $T_{Ca\text{-}in\text{-}opx}$ is 816–1124. There is generally good agreement with no systematic difference observed between the two thermometers for almost all of the samples (Table 7; Fig. 7a). Analytical uncertainties propagated through the thermometer equations produce temperature uncertainties in the region of about 10 °C for T_{BK} and 15 °C for $T_{Ca\text{-}in\text{-}opx}$.

For comparison, we have also used the empirical thermometer of Witt-Eickschein and Seck (1991), which is based on Cr–Al exchange between orthopyroxene and spinel. Temperature estimates for the peridotites using this geothermometer give a range of between 829 and 1129 °C (Table 7). The agreement among temperatures obtained using different thermometers is satisfactory and for most of the xenoliths the differences between core temperatures obtained using the Ca-in-orthopyroxene and the other ther-

Table 7
Equilibrium temperatures, pressures and oxygen fugacities calculated for the peridotite xenoliths from NW Turkey

Sample numbers	$T_{Ca\text{-}in\text{-}opx}$ (°C)[a]	T_{BK} (°C)[b]	$T_{Al\text{–}Cr\text{-}opx}$ (°C)[c]	$P_{Ca\text{-}in\text{-}ol}$ (GPa)[d]	$\Delta_{\log} f_{O_2}^{FMQ}$
XE7A	1010	1023	972		−1.52
XE2	831	811	842	1.49	−1.27
XE2C	954	983	945		−1.32
XE2B	941	981	917	1.82	−1.41
XE7B	995	1002	926	1.78	−1.15
XE1B	949	999	911	1.72	−0.54
XE11	995	1010	985	1.82	−0.94
XE1A	892	907	901	1.52	−0.48
XE14	988	1049	964	1.65	−0.79
XE2A	913	962	874		−0.95
XE13A	1103	1127	1076	1.97	−0.53
XE10	1124	1178	1129	2.10	−0.78
XE13	1117	1138	1121	1.82	−0.76
XE13B	1048	1059	1021	1.96	−0.17
XE8	866	887	836		0.05
XE5	916	966	899		−0.17
XE4	878	892	851		−0.32
XE3	920	937	893	1.68	0.08
XE1	911	921	886	1.62	−0.15
XE6	816	864	829	1.61	0.14

Temperatures were calculated using the geothermometers of Brey and Köhler (1990) at an assumed pressure of 2.0 GPa, and pressures were calculated with the Ca-in-olivine geobarometer of Köhler and Brey (1990). Oxygen fugacities calculated relative to the FMQ buffer, using the method of Ballhaus et al., (1991), using T_{BKN} and pressures set at 2.0 GPa.

[a] Ca-in-opx thermometer (Brey and Köhler, 1990).
[b] Two pyroxene thermometer (Brey and Köhler, 1990).
[c] Al–Cr-opx thermometer (Witt-Eickschein and Seck, 1991).
[d] Ca-in-olivine geobarometer (Köhler and Brey, 1990).

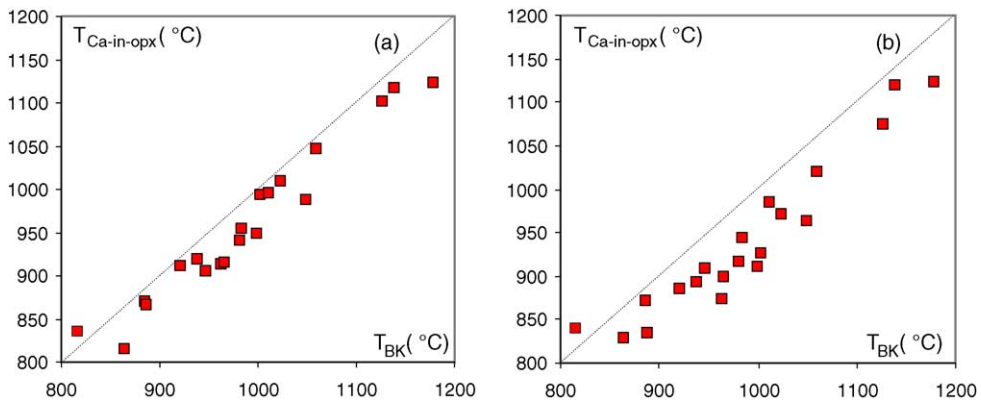

Fig. 7. Plots of temperature estimates for mantle xenoliths of NW Turkey from the two pyroxene geothermometer of Brey and Köhler (1990) (T_{BK}) vs. (a) Ca-in-opx thermometer of Brey and Köhler (1990) ($T_{Ca\text{-}in\text{-}opx}$) and (b) Al–Cr-opx thermometer of Witt-Eickschein and Seck (1991) ($T_{Al\text{–}Cr\text{-}opx}$).

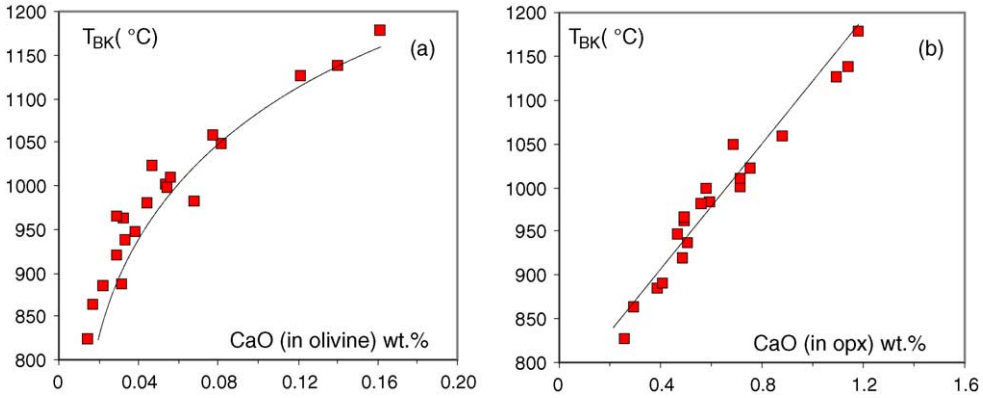

Fig. 8. The relationship between temperature and Calcium contents in (a) olivine and (b) orthopyroxene in spinel-lherzolite xenoliths from NW Turkey.

mometers were insignificant or even non-existed, suggesting that the xenoliths were equilibrated under ambient pressure and temperature conditions (Fig. 7a and b).

6.2. Equilibration pressures of the xenoliths

For garnet peridotites, a variety of precise geobarometers have been derived based on chemical changes on coexisting minerals which are quite sensitive to pressure, and for which reliable thermodynamic data exist (Brey and Köhler, 1990 and references therein). However, geobarometry of spinel peridotites is far more difficult than that of garnet peridotite. The absence of garnet and plagioclase constrains the equilibrium pressures of the peridotite nodules from NW Turkey to lie within the range of the spinel stability field that was constrained by: (1) the maximum pressure limit of plagioclase-bearing peridotites (Green and Hibberson, 1970; Obata, 1976; Herzberg, 1978; O'Neill, 1981; Gasparik, 1984, 1987); and (2) the minimum pressure limit for the appearance of garnet calculated from spinel compositions according to Webb and Wood (1986). This would approximate a pressure interval of between about 1.0 and 2.2 GPa (e.g. Webb and Wood, 1986), corresponding to depths of 30 and 60 km.

The geobarometers proposed by Köhler and Brey (1990), and Adams and Bishop (1982, 1986) may also provide an approximation to estimate equilibration pressures of spinel-peridotite xenoliths as they are based on the exchange of equilibrium Ca between olivine and clinopyroxene. Such an exchange relationship, basically a function of pressure is, however, very sensitive with respect to temperature. Mean values of T_{BK} and $T_{Ca\text{-}in\text{-}opx}$ estimates in individual samples were used as input temperatures to the Ca-in-olivine geobarometer in an effort to avoid the magnification of errors as a result of the large temperature dependence of the barometer. The wide range in olivine (and orthopyroxene) CaO in our xenolith suite shows the positive relationship between CaO and temperature (Fig. 8) as is expected as determined from experimental studies (e.g. Köhler and Brey, 1990). For a small number of samples, however, the calculated pressure range exceeds that for the spinel-peridotite stability field. Considering the high diffusion velocity of Ca in olivine compared to that in pyroxenes, the reliability of this barometer is strongly dependent on the state of equilibrium in each particular sample. Disequilibrium effects may be responsible for unrealistically low-pressure estimates obtained from some of the mineral grains, which are excluded from the average estimate of equilibration pressures.

In the view of the extremely low Ca content of the olivines (<0.1 wt.%), and the large influence that variation in Ca has on the calculated pressure, careful attention was paid to determining Ca as a trace element using the electron microprobe. Background and peak positions were carefully selected and long counting times were used to obtain counting statistic errors of 0.005 wt.% (2σ) and detection limits of 0.004 wt.% (99% confidence level). Uncertainties in calculated pressures using these estimates of precision propagated through the pressure algorithms by Brey and Köhler (1990) are the order of 0.3 GPa.

For the spinel-peridotites from NW Turkey, reasonable estimates of equilibrium pressures obtained using the Köhler and Brey (1990) geobarometer, which is a refined Adams and Bishop (1982, 1986) geobarometer, are reported in Table 7 and range from 1.49 to 2.10 GPa, corresponding to a depth of approximately 50–73 km. The estimated pressure interval stays well within the experimentally determined stability field for spinel-lherzolites (e.g. O'Neill, 1981).

6.3. Oxygen fugacity

A number of calibrations of mineral reactions have been widely applied to spinel peridotite xenoliths as a method to estimate the redox state of the upper mantle (e.g. Wood, 1990; Ballhaus et al., 1991). We have applied the oxygen barometer formulation of Ballhaus et al. (1991) to calculate oxygen fugacities for the peridotite xenoliths from the electron microprobe data. Although the ferric iron content of the spinels can be determined with adequate precision from electron microprobe data by calculation, particularly for relatively oxidized spinels, the introduction of systematic errors as a result of varying analytical routines may render these calculations unreliable in the absence of adequate calibration or secondary standardization (e.g. Wood, 1990). Despite the potential pitfalls, the broad elements of mantle f_{O_2} variation were established using routine electron microprobe data (e.g. Ballhaus et al., 1991) and have not changed substantially with direct determinations of Fe^{3+} in spinel. The conclusions derived from microprobe data have thus proved useful in the past and are furthermore most robust for relatively Fe^{3+}-rich spinels, where the effects of systematic inaccuracies are least significant.

Calculated oxygen fugacities are given in Table 7 relative to the FMQ (fayalite–magnetite-quartz) buffer at 2.0 GPa to facilitate comparisons with previously published data. The oxygen fugacity relative to FMQ is little affected by errors in pressure within the range of the spinel-lherzolite stability field (Wood, 1990). Changing the pressure to 1.5 GPa causes a shift on Δf_{O_2} of <0.001 log units. Oxygen fugacities of the xenoliths from NW Turkey fall in a relatively narrow range straddling the FMQ buffer ($\Delta_{\log} f_{O_2}^{FMQ} = -0.15$ to 0.08). These values are within the reported range for continental xenoliths, but for some of the samples slightly more oxidized than average. It is apparent that the fertile, unmetasomatized lherzolites and most harzburgites are moderately reduced with their oxidation states similar to the values reported by Ballhaus (1993) for primitive spinel peridotites from undisturbed subcontinental lithosphere (Fig. 9). The more depleted dunites, however, although recording similar f_{O_2} conditions, are relatively more oxidized and lie slightly above this field (toward FMQ) in terms of Cr# $-\Delta_{\log} f_{O_2}^{FMQ}$ relations (Fig. 9), close to a composition space represented in the literature by xenoliths from oceanic arc and supra-subduction zone mantle. More pronounced oxidation conditions of the depleted peridotites might be attributed to a possible melt/solid reaction associated with extensive porous flow in dunite channels.

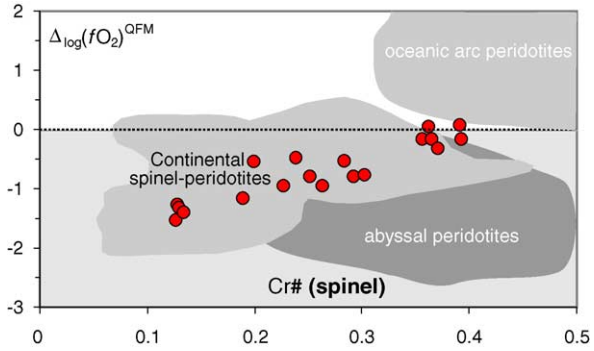

Fig. 9. Plot of $\Delta_{\log} f_{O_2}^{FMQ}$ against Cr# of spinel for the peridotite xenoliths from NW Turkey. The approximate fields for abyssal peridotites, oceanic arc peridotites and peridotites from subcontinental lithosphere (e.g. Ballhaus, 1993) are shown for reference.

6.4. Inferring the liquidus temperatures of the alkali primary melts

The xenolith-bearing lava flows in NW Turkey are dominantly alkali basalts, i.e. nepheline-normative magmas, which vary from basanites with 15% modal olivine to olivine-phyric alkali basalts. The published bulk-rock chemical data show that the erupted lavas are relatively free of the complicating effects of mantle lithosphere or crustal interactions and several of these lavas have bulk compositions that may approximate primitive melts (Aldanmaz et al., 2000; Yilmaz and Polat, 1998). Although the occurrence of olivine-rich basanitic rocks does not necessarily prove that Mg-rich primary melts existed because the rocks may consist of relatively Mg-poor melt with accumulated olivine crystals, the mineral chemical data indicate a strong correlation between the calcium content of olivine and the magma composition such that the most magnesian samples represent the low-Ca end of the spectrum. In addition the magnesian olivines were $>Mg\#_{0.83}$ in all cases and reached $Mg\#_{0.91}$ for the most magnesian samples. It is evident from the correlation between CaO and Mg# (e.g. contrasting with the low-Ca content in olivine of spinel-peridotite xenoliths), and from the equilibrium between olivine phenocrysts and host rocks (Fig. 6a), that the magnesian olivines are compositionally unimodal phenocrysts from a related suite of magmatic origin, and not xenocrysts from mantle sources (Table 7). Thus, Fig. 6b shows that the CaO contents of all our olivine analyses from the alkaline lavas behave as a single series, when plotted as a function of Mg#. The slight fall in average CaO with increasing olivine Mg# fits the experimentally based model of Libourel (1999) in that both the forsterite content of the olivine and the magma CaO content are major controls on olivine CaO. The CaO contents of the phenocrysts from the alkaline lavas of NW Turkey are clearly far above the range for mantle xenoliths (and also xenocrysts), because possible mantle xenocrysts would have very low (less than 0.2%) contents of CaO (Fig. 6b).

It is possible to use the data on the compositions of alkaline rocks from NW Turkey to identify the most primitive magmas and to determine their temperatures of eruption. In this context, for instance, the formulation of a relationship between 'liquidus' temperature and the major element composition of primary liquid (e.g. the 'Ford' geothermometer of Ford et al., 1983) allow the estimation of anhydrous liquidus temperature for primary magmas directly from their major element compositions.

However, it should be noted that the erupted lavas have most probably been modified from their primary compositions during their ascent to the surface. To calculate primary melts we need to correct for this modification. Fractional crystallization is probably the most important of these processes. At low pressures,

fractionating phases from basaltic liquids are generally olivine, then plagioclase, and then clinopyroxene. At higher pressures (e.g. >0.5 GPa), clinopyroxene tends to appear earlier than plagioclase, or, in certain conditions, plagioclase does not even crystallize as a phenocryst phase. It is difficult to accurately correct for multi-phase crystal fractionation, and it is common to apply up-temperature correction only to MgO-rich samples by incrementally adding equilibrium olivine, assuming that olivine was the only fractionating phase (e.g. Fram and Lesher, 1997). To circumvent such difficulties and be able to assess the primary melt composition accurately, we have selected the high-MgO samples, for which olivine appears to be the only fractionation phase. The procedure that we have used for the purpose of calculating the primary melt compositions is to: (1) calculate olivine composition in equilibrium with liquid using an Fe–Mg exchange coefficient, $K_D^{Fe–Mg}$, and the Ni partition coefficient, ${}^{ol/liq}D_{Ni}$; (2) add 0.1 wt.% of the equilibrium olivine to liquid; and (3) repeat (1) and (2) in successive steps until the equilibrium olivine has the same composition as the mantle olivine (e.g. Fo_{91}, Albaréde, 1992; or until the Ni content of equilibrium olivine reaches 3500 ppm).

To apply olivine fractionation correction, we have selected the samples that are aphyric and have MgO >8 wt.%. Despite a large number of geochemical data sets from the alkaline volcanic province of NW Turkey, the number of samples that satisfy these conditions is limited. When a modal analysis is given, we classified samples with less than 5% phenocrysts as aphyric. All data are normalized on an anhydrous basis, and $Fe^{2+}/\Sigma Fe$ of 0.9 is assumed (Herzberg and O'Hara, 2002). A constant $K_D^{Fe–Mg}$ of 0.3 is used to calculate equilibrium olivine composition; changing this value by ±0.01 has only minor influence on our results. From the Fe/Mg partitioning relationship between olivine and liquid (e.g. Roeder and Emslie, 1970; Ulmer, 1989), it is also possible to estimate liquidus olivine composition for a particular bulk-rock composition.

In Table 8, we have listed calculated primary melt compositions for the alkaline volcanic rocks from NW Turkey along with the forsterite content of the liquidus olivine for that bulk composition. The calculated primary or parental melts that formed the most magnesian composition have around 13–16 wt.% MgO. This calculation assumes an oxidation state of FMQ + 0.5 log units and incrementally redissolves equilibrium olivine in 0.01% increments using the PETROLOG program (Danyushevsky et al., 2000). Using the Ford geothermometer, the liquidus temperature is calculated for the most magnesian samples from the NW Turkish alkaline suite, which range from ∼1330 to ∼1410 °C (Table 8).

The calculated parental melts contain MgO similar to or slightly higher than the bulk rocks. The differences are also insignificant for elements that are incompatible during olivine fractionation, and all ratios of such elements (e.g. CaO/Al_2O_3) are preserved. The major difference between the calculated melts and the bulk rocks lies in FeO, this being 0.5–1 wt.% lower in the calculated liquid than in the bulk rocks. The reason for this may be that the equilibrium olivines added in the calculations become successively more Fe-poor, and in liquids with more than ∼12 wt.% MgO the added olivines contain less iron than the liquid. These Mg-rich, Fe-poor olivines constitute a major part of the olivine assemblage in the calculated liquids, whereas the olivines in the bulk rocks are more Fe-rich, with a frequency peak at $Mg\#_{0.87–0.89}$.

Using the major element compositions of basaltic parental primary melts, it is also possible to place constraints on the range of pressures, at which melt segregation from the source mantle has taken place. A considerable weight of experimental evidence demonstrates the dependence of the bulk composition of primary mantle melts on pressure (e.g. Kushiro, 1998; Hirose and Kushiro, 1993) and suggests that silica-undersaturated alkaline magmas originate from a relatively deep source. Equations that relate bulk rock SiO_2 contents to the pressure of melting based on peridotite melting experiments have been suggested

Table 8
Calculated compositions, temperatures and pressures of parental melts and primary melt segregations for the compositions of mafic alkaline lavas from NW Turkey

Sample	EA517	EA516	EA520	EA509	EA511	EA512	EA252
SiO_2	44.847	44.668	44.985	46.225	44.614	48.375	45.201
TiO_2	2.613	2.569	2.557	2.654	2.516	2.624	2.676
Al_2O_3	11.487	11.350	12.490	11.987	11.301	13.303	12.651
Fe_2O_3	1.545	1.559	1.524	1.442	1.617	1.564	1.657
FeO	9.682	9.612	10.039	9.587	9.543	9.567	10.700
MnO	0.157	0.156	0.158	0.147	0.155	0.145	0.161
MgO	15.099	15.669	12.562	13.817	15.441	8.805	11.288
CaO	8.992	8.908	10.604	8.853	8.601	9.653	9.786
Na_2O	3.356	3.253	3.090	2.987	3.328	3.747	3.574
K_2O	1.243	1.299	0.839	1.528	2.051	1.559	1.437
P_2O_5	0.881	0.86	0.701	0.676	0.735	0.562	0.775
Cr_2O_3	0.098	0.098	0.099	0.098	0.097	0.097	0.095
Total	100.000	100.001	99.648	100.001	99.999	100.001	100.001
Fo	91.09	91.47	88.57	90.15	91.49	84.99	87.15
Temperatures and pressures of parental melts							
T (°C)[a]	1397.5	1408.7	1330.8	1366.9	1416.4	1255.2	1315.1
P (GPa)[b]	1.3	1.4	1.1	1.1	1.4	1.1	1.2
Temperatures and pressures of primary melt segregations							
T (°C)[c]	1432.8	1448.4	1365.6	1389.2	1443.2	1287.0	1328.7
P (GPa)[c]	2.9	3.0	2.4	2.2	3.0	1.1	2.1

Melts calculated by addition of equilibrium olivine in 0.5% increments to the matrix compositions of the lavas. Temperature and pressure of melt segregation have been estimated using the approach of Ford et al. (1983) and Albaréde (1992).

[a] From Ford et al. (1983).

[b] Model dependent: assuming a pressure increase of 0.2 kbar per 0.5% olivine added.

[c] From Albarede (1992) Eqs. (2) and (3).

by several researchers and applied to estimate the depth of basaltic magma sources (e.g. Kushiro, 1998). The least differentiated mafic compositions (e.g. basanites with the most magnesian olivine phenocrysts; 88.5–91.4% Mg_2SiO_4) from the alkaline volcanic suites of NW Turkey have 44–46 wt.% SiO_2 and these values correspond to pressures of 2.4–3.1 GPa using the pressure–composition regressions given in the sources cited, although some alkaline basalt samples yield lower pressure estimates. Assuming an average thickness of 30 km for the continental crust (e.g. Saunders et al., 1998) with an average density of 2800 kg m^{-3}, and a density of 3240 kg m^{-3} for the upper mantle, estimated pressures correspond to depths of roughly 90–118 km. Segregation pressures for the primary melts have also been estimated using the approach by Herzberg (1978) and Herzberg and Zang (1996) at 2.2–3.1 GPa, based on bulk-rock CaO/Al_2O_3, and at 2.1–3.0 GPa using the simple algorithm of Albaréde (1992). Differences between the pressure estimates by different approaches are within error and for the relevant temperatures calculated these estimates correspond to mantle potential temperature of ∼1300 °C.

If the minimum pressures of melt segregation were ∼2.0–2.5 GPa, then melts segregated at ∼90–80 km depth, indicating a lithospheric lid thickness of ∼80 km that curtailed the melting column. The melts thus ascended through roughly 80 km of conduit system in the lithospheric mantle and crust producing final melts with variable amounts and compositions of olivine phenocrysts ranging from $Mg\#_{0.83–0.91}$. At high

magma ascent rates many olivine crystals were probably kept in suspension all the way to the surface, whereas at low ascent rates only few and small olivines were suspended and the magmas erupted as olivine-microphyric or aphyric lavas. Pulsating magma ascent would probably lead to mixing of magma batches in various stages of fractionation and equilibration. In stagnating magma pockets crystallization proceeded to low Mg-olivines ($Mg\#_{0.83–0.87}$), but the majority of the magmas passed through the crust rapidly that equilibration was far from complete. The chemical composition of the latter may thus be used to constrain the melting conditions of the mantle source region.

7. Thermal state of the upper mantle beneath NW Turkey

The thermal state of the upper mantle can be assessed from the application of experimentally based thermobarometry methods to appropriate suites of xenoliths. Estimates of equilibration temperature and pressure for individual xenoliths can constrain local geothermal gradients at the time of eruption that carried the xenoliths to the surface.

We have derived the *P–T* conditions of spinel peridotites from NW Turkey using the combination of the geothermometer of Brey and Köhler (1990) and geobarometer of Köhler and Brey (1990). This preferred data set is plotted in Fig. 10, which also shows experimentally determined phase boundaries between garnet-, spinel- and plagioclase-lherzolites in the CaO–Fe–MgO–Al_2O_3–SiO_2–Cr_2O_3 (CFMASCr) system with a fixed olivine composition of $Fo_{0.90}$, and Cr/(Cr + Al) ratios in spinel ranging from 0 to 0.4 (O'Neill, 1981). The spinels in the xenoliths in this study have Cr/(Cr + Al) ratios of 0.1–0.4. All of the spinel peridotites from NW Turkey fall in the experimentally determined spinel-lherzolite field in the CFMASCr system.

The geotherm constructed for the NW Turkish peridotite xenoliths is shown in Fig. 10, together with two curves of conductive geotherms in the continental lithosphere for heat flow of 60 and 90 mW m^{-2}, respectively (e.g. Pollack and Chapman, 1977). The xenolith-derived geotherm for NW Turkey is reasonably well constrained and passes through 810 °C at ~1.4 GPa and 1180 °C at ~2.1 GPa. The temperature-depth array recorded by the xenoliths resembles that of many similar spinel peridotite suites from continental alkaline basalt occurrences (e.g. Mercier, 1980). If interpreted in a steady state context, the observed pressure–temperature relations translate to the surface heat flux of ~85–90 mW m^{-2}. The observed *P–T* array suggest that the parts of lithospheric mantle has been sampled continuously from depths of 50 to 80 km. Extrapolation of the *P–T* data array to the adiabatic upwelling of normal temperature asthenospheric mantle (e.g. McKenzie and Bickle, 1988; McKenzie and O'Nions, 1991) results in an apparent lithospheric thickness of ~80 km at the time of basaltic melt extraction. The occurrence of high-temperature for peridotites of spinel facies stability zone (~1180 °C) is indicative for a high geothermal gradient. The geothermal gradient beneath NW Turkey can thus be interpreted to be greater than that of conductive model for stable continents, thereby suggesting a perturbation of thermal structure of the uppermost mantle.

8. Discussion: melting history and equilibration temperatures

Most of the compositional relationships among the minerals comprising the lherzolite and most harzburgite xenoliths as well as some between minerals and whole-rocks (xenoliths) indicate that these peridotites

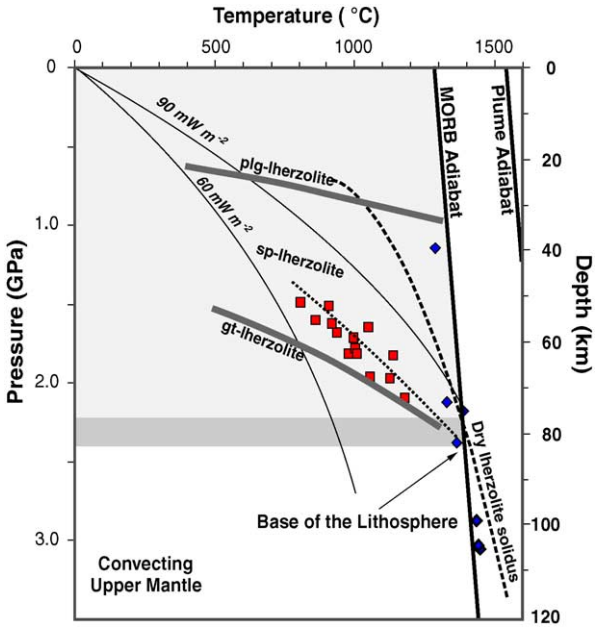

Fig. 10. Observed depth and temperature for xenoliths from NW Turkey. Depth as a function of pressure is $[P - \rho_c g Z_c]/[(\rho g) + Z_c]$, where the crustal density ρ_c is 2800 km m^{-3}, the crustal thickness is 30 km, and the mantle density ρ is 3400 km m^{-3}. Squares represent coarse, shallow xenoliths along which the inferred (and laterally averaged) regional geotherm was determined (the dashed line). Closed diamonds represent alkaline primary melts along which the inferred ambient mantle geotherm was determined. The MORB adiabat and the plume adiabat have gradients of 0.3 K km^{-1} and they have the potential temperatures of 1280 and 1540 °C, respectively (T_p; projected along the solid-state adiabat to one atmosphere). Plg-Lherzolite, Sp-Lherzolite and Gt-Lherzolite denote experimentally determined stability fields for plagioclase, spinel and garnet, respectively. Dry peridotite solidus shown as dashed curve are from Herzberg et al. (2000). Conductive Continental Geotherm curves are from Pollack and Chapman (1977).

were sampled from parts of the mantle that underwent varying degrees of melting and basaltic melt extraction. These include the general increasing of spinel Cr# with increasing silicate-phase Mg# and Cr_2O_3 abundances. Further evidence suggesting that the xenoliths are the products of varying degrees of mantle melting is their variable depletion in fusible elements such as Ti, Ca, Al and Na compared to the estimated primitive mantle composition (e.g. McDonough and Sun, 1995) (Fig. 2). Although there are some samples with fertile major element compositions, the majority of the rocks are characterized by refractory major element chemistry (i.e. Al_2O_3, TiO_2 and CaO all correlate negatively with MgO) and have high Mg# (0.910–0.915) suggesting that they are melt-depleted residues. The samples are also characterized by near-constant CaO/Al_2O_3 ratios consistent with continuous melt extraction from the source. The samples are spinel-lherzolites, -harzburgites and -dunites with highly forsteritic olivines ($Fo_{0.896–0.914}$). Whole rock Mg# and spinel Cr# indicate a shift toward higher values for the harzburgites (compared to lherzolites) consistent with their larger degree of depletion.

The inverse correlations between SiO_2, Al_2O_3, CaO, TiO_2, Na_2O and MgO in the peridotites are quantitatively consistent with the variable amount of extraction of basaltic melts. As is shown in Fig. 2, when the major element compositions of the peridotites are compared to polybaric batch melting model trends calculated using the MELTS thermodynamic approach (Ghiorso and Sack, 1995), the element

variations seem to be consistent with the calculated trends of experimental results, supporting the residual origin for the xenoliths from partial melting of spinel-lherzolites. The increase of the refractory character of the peridotites within the alkaline suite is accompanied by a decrease of the modal abundances of pyroxene and increase of those of olivine and Mg# of whole rocks. Similar characteristics are generally interpreted in terms of variable degrees of progressive partial melting of a relatively fertile upper mantle and melt extraction (Bodinier et al., 1991). Application of the numerical expression (e.g. Hellebrand et al., 2001) based on the spinel Cr# (e.g. with increasing degree of partial melting, decreasing activity of aluminum in peridotite leads to an increase in equilibrium Cr# in spinel) also indicates that the xenoliths are likely to be the residual products formed after 3.2–14.8% basaltic melt extraction from a mantle source with variable degrees of fertility (Table 8; Fig. 5a and b).

As all xenoliths within the alkaline lavas are spinel-peridotite, and because one of our main objectives is to evaluate the thermal structure beneath the region, we can estimate a minimum gradient by first assigning the large equilibrium temperature range as an overprint on the spinel-peridotite stability field of the upper mantle at the time of basaltic melt extraction. There is no reliable and widely applicable method for precise determination of equilibration pressures for spinel peridotite; the quantitative constraint of equilibrium pressure is very much depending on the analytical uncertainty during mineral analyses. We can, however, using both the regional heat flow and mineral stability constraints, assign the lowest equilibrium temperatures observed as representing the uppermost part of the mantle-sampling zone within the spinel-peridotite stability conditions and compare this result with the quantitative estimates of equilibrium pressures by Ca-in-olivine geobarometer. A reasonable approximation of this temperature, at ∼1.4 GPa, is about 810 °C (Fig. 10).

In the absence of garnet peridotite, the high end of the equilibrium temperature range (∼1180 °C) can be assigned to represent the minimum depth for the transition of spinel-peridotite to garnet-peridotite stability zone. Experimental determinations for the spinel to garnet phase boundary show that this is ∼2.1 GPa (e.g. O'Neill, 1981; Webb and Wood, 1986; Klemme and O'Neill, 2000) and this result is also consistent (within error) with the results of pressure estimates obtained using the Ca-in-olivine geobarometer applied in this study. Combining the ∼80 km depth for high equilibrium temperature xenoliths with the ∼45 km depth for low equilibrium temperature xenoliths yields an average temperature gradient for the uppermost mantle at the time of Cenozoic basaltic melt eruption. That is, when considering that spinel peridotite is stable throughout an approximately 40 km zone of upper mantle, the constructed geotherm is ∼14 °C km^{-1}. This corresponds to about 85–90 mW m^{-2}, a value notably grater than geotherms observed for stable continents, which generally manifest heat flows smaller than 60 mW m^{-2} (e.g. Chapman, 1986), but rather close to the average value of conventional conductive model (90 mW m^{-2}) for areas of crustal extension with relatively thinned lithosphere (e.g. Pollack and Chapman, 1977).

The elevated xenolith-derived conductive geotherms are, in many cases, suggested to have resulted from a possible thermal perturbation by deep-seated thermal anomalies associated with mantle plumes that characterize the areas with mantle potential temperatures (T_p) of 1450 °C or higher. In this context, many suggest that impingement of an upwelling mantle plume on the base of the lithosphere may result in generating partial melts of mantle origin as well as in perturbing the thermal structure of the lithospheric lid above the plume (e.g. Thompson and Gibson, 2000). Major-trace element and isotope geochemical signatures of the xenolith-bearing alkaline lavas in NW Turkey have been shown to be closely resemble to those of oceanic island basalt (OIB)-type lavas (e.g. Aldanmaz et al., 2000; Yilmaz and Polat, 1999), the formation of which is usually interpreted as sampling a hot spot source with mantle potential temperature 250–300 °C higher than that of normal temperature astenospheric mantle (e.g. Davies, 1999). Thus, on

the basis of geochemical characteristics of the lavas, the main stage of alkaline magma production in the volcanic suite of NW Turkey could be interpreted to have resulted from a plume activity.

However, there are numerous problems reconciling the observations with a plume model in NW Turkey. Extensional stress associated with the lithospheric uplift, for instance, should be the maximum above a plume apex, which in turn would be expected to create an uplift and doming structure as a surface manifestation of such thermal anomaly. This is, however, not observed in the alkaline volcanic field of NW Turkey. Pinpoint thermal and stress perturbation which would be generated by adiabatically upwelling mantle plume is also inconsistent with linearly distributed patterns of the volcanic centers as well as planar geometry of normal or even strike-slip faulting of NW Turkey, where the small volume and discontinues (or episodic) alkaline magma generation is related mostly to strike-slip (or transcurrent) deformation.

Another strong argument against a mantle plume origin for the relatively elevated thermal gradient beneath NW Turkey is provided from the evidence by liquidus temperatures of the primary alkaline melts. The bulk chemistry of the undifferentiated (or fractionation corrected) alkaline magma compositions from NW Turkey provides evidence for primary melts with 11–16 wt.% MgO and liquidus temperatures ranging from 1290 to 1410 °C. Combining these results with the information of the depth of melt extraction imply that the mantle region which melted to produce the alkaline primary compositions has potential temperature of ∼1300 °C (Fig. 10), a value that is significantly lower than the suggested values for deep-seated thermal anomalies associated with mantle plumes ($T_p > 1450$ °C; McKenzie and Bickle, 1988; Davies, 1999).

An alternative, and much more likely, explanation would be that the moderately elevated xenolith-derived conductive geotherm may have resulted from a possible thermal perturbation by the convective heat transport related to the lithospheric thinning accompanying upwelling of hot asthenosphere. Such a model may particularly be important in cases when the thermal structure of the mantle lithosphere has a profile that cannot be reconciled with simple conduction models, but falls far above it even at shallow depths. Considering the fact that the area has been influenced by active extensional forces since at least the Middle Miocene, a likely explanation would be that the relatively high geotherm of 85–90 mW m^{-2}, or that yielding ∼1180 °C at ∼2.1 GPa, largely represents thermal perturbation by impingement of hotter, upwelling asthenosphere resulted from thinning of the lithosphere during the Late Cenozoic (Fig. 11).

However, the absence of alkaline volcanic activity in many other extensional basins of western Turkey during the Late Miocene and seismic evidence (e.g. moderately efficient *Sn* propagation; Gök et al., 2000) suggest that the melt generation beneath the region is difficult to be explained solely by large-scale lithospheric thinning and thermal uplift. Heat flow density measurements across the area also show that the thermal gradient in much of NW Turkey is not anomalously high (e.g. Pfister et al., 1998) and only locally reaches up to the values obtained using the xenolith-derived geotherms. It, thus, appears more plausible that the thermal gradient provided by the xenolith-derived geotherm represents the local mantle region, leading to the suggestion that the Late Miocene alkaline volcanism of NW Turkey is not only related to regional extensional opening of the area but is also partly controlled by local thermal perturbations and upwelling of shallow asthenospheric mantle materials along the lithospheric scale major shear zones. In this context, isentropic decompression melting of mantle peridotites under dry conditions can be considered as an efficient mechanism to produce basaltic melts along the lithospheric scale major shear zones, where a significant component of vertical flow and instantaneous upraise of asthenospheric mantle material would cause a part of the mantle asthenosphere exceeds its solidi (Fig. 11). The resultant melts

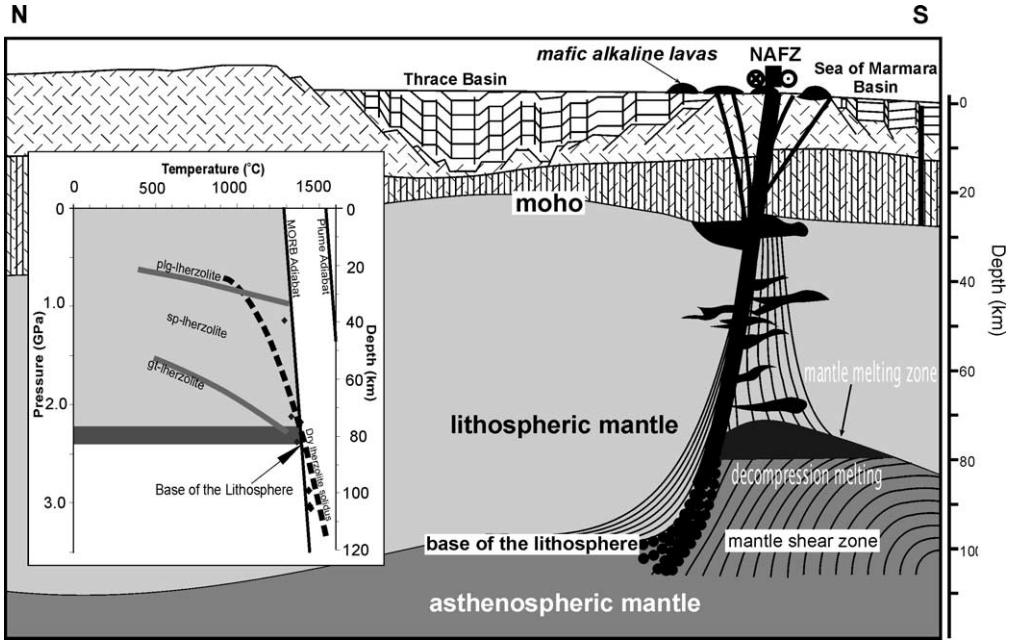

Fig. 11. Schematic diagram illustrating the magma genetic model for the Late Miocene alkaline volcanic province of NW Turkey. The inferred model has been deduced from the petrological and geochemical data. NAF, North Anatolian Transfom Fault Zone.

would then continue their rapid assent through lithospheric fracture zones, during which they sample parts of the lithospheric mantle from across a depth of about 80 km.

9. Concluding remarks

In NW Turkey, extension-related mafic alkaline magmas were erupted episodically during much of the Late Miocene. Several of these magmas entrained deep-seated ultramafic xenoliths that provide important constraints on the composition and thermal structure of the upper mantle beneath the region. Most of the intra-grain compositional variations reflect thermal processes characterizing ambient conditions in the upper mantle. A large proportion of the xenoliths are characterized by homogeneous mineral compositions and show consistent compositional correlations between constituent phases. These characteristics indicate that the xenoliths can be regarded as equilibrated under the prevailing pressure–temperature conditions. Geothermobarometric calculations on these xenoliths yielded equilibrium temperatures ranging from about 810 to 1180 °C pointing to a provenance depth ranging from 45 km (1.4 GPa) to 80 km (2.1 GPa). The later value should approximate the thickness of the lithosphere beneath the area. The results of thermobarometry reveal a moderately hot upper mantle and are in agreement with the local surface heat flow data.

The geothermal gradients constrained by xenoliths indicate thermal perturbations in the lithosphere probably related to the impingement of upwelling sub-lithospheric sources. These data, however, suggest that any asthenospheric intrusion into the lithosphere should be limited to depths greater than 70 km. Nevertheless, the absence of alkaline volcanic activity in many of the other extensional basins of western

Turkey during the Late Miocene period and seismic evidence is not consistent with large-scale lithospheric thinning and thermal uplift. It appears more plausible that the Late Miocene alkaline volcanism of NW Turkey are not only related to regional extensional opening of the area but are also partly controlled by local thermal perturbations and upwelling of shallow astenospheric mantle materials along the lithospheric scale major shear zones (e.g. the North Anatolian Transform Fault). We thus propose that lithospheric scale strike-slip deformation could have promoted transtension-related decompression melting of sub-lithospheric mantle that had already been decompressed by regional extensional process. Thermo-barometric calculations indicate that both high-*T* and low-*T* xenoliths are included within a single volcanic vent, suggesting that the xenoliths may originate in a shear zone probably due to uplift of hot mantle material into cooler uppermost mantle.

P–T estimates on the alkaline melts from NW Turkey requires that much of the melt was last in equilibrium with its mantle host in either the spinel stability field or near garnet-spinel transition zone. It rules out an origin from deeper mantle sources, meaning that the melt probably comes from 80 to 100 km depth or near the base of the lithosphere. High forsterite contents of euhedral, undeformed olivine phenocrysts in the most primitive alkaline lavas show that their parental melts had MgO contents significantly greater than that of the moderately evolved lavas that dominate the alkaline suite. Olivines with $Fo_{89.6.5–91.4}$ cores dominate the phenocryst populations of the most primary compositions. Melts in equilibrium with the forsteritic olivines in these rocks would have 11–16% MgO (assuming $Fe^{2+}/\Sigma Fe = 0.9$; $K_D = 0.3$), and they would have liquidus temperatures of ∼1290 to 1410 °C. For the relevant segregation pressure estimates, these values correspond to mantle potential temperature of ∼1300 °C.

Acknowledgments

We thank Pete Hill for providing access to the electron probe facilities at Edinburgh University, Brian Cousens and Giovanni Piccardo for detailed and constructive reviews, and Giorgio Ranalli for much helpful editorial handling. This work was financially supported by TUBITAK grant YDABAG-102Y069.

References

Adams, G.E., Bishop, F.C., 1982. Experimental investigation of Ca–Mg exchange between olivine, orthopyroxene and clinopyroxene: potential for geobarometry. Earth Planet. Sci. Lett. 57, 241–250.

Adams, G.E., Bishop, F.C., 1986. The olivine-clinopyroxene geobarometer: experimental results in the CaO–FeO–MgO–SiO_2 system. Contrib. Miner. Petrol. 94, 230–237.

Albaréde, F., 1992. How deep do common basalts form and differentiate? J. Geophys. Res. 97, 10997–11009.

Aldanmaz, E., 2002. Mantle source characteristics of alkali basalts and basanites in an extensional intracontinental plate setting, western Anatolia, Turkey: implications for multi-stage melting. Int. Geol. Rev. 44, 440–457.

Aldanmaz, E., Pearce, J.A., Thirlwall, M.F., Mitchell, J.G., 2000. Petrogenetic evolution of late cenozoic, post-collision volcanism in Western Anatolia, Turkey. J. Volcanol. Geother. Res. 102, 67–95.

Arai, S., 1992. Chemistry of chromian spinel in volcanic rocks as a potential guide to magma chemistry. Miner. Magazine 56, 173–184.

Asimow, P.D., Hirschmann, M.M., Stolper, E.M., 1997. An analysis of variations in isentropic melt productivity. Philos. Trans. R. Soc. Lond. Ser. A 335, 255–281.

Ballhaus, C., 1993. Redox states of lithospheric and asthenospheric upper mantle. Contrib. Miner. Petrol. 114, 331–348.

Ballhaus, C., Berry, R.G., Green, D.H., 1991. High-pressure experimental calibration of the olivine-orthopyroxene-spinel oxygen geobarometer: implications for the oxidation state of the upper mantle. Contrib. Miner. Petrol. 107, 27–40.

Bayrak, M., Gurer, A., Gurer, O.F., 2004. Electromagnetic imaging of the Thrace basin and Intra-Pontide subduction zone Northwestern Turkey. Int. Geol. Rev. 46, 64–74.

Bertrand, P., Mercier, J.-C., 1985. The mutual solubility of coexisting ortho- and clinopyroxene: toward an absolute geothermometer for the natural system? Earth Planet. Sci. Lett. 76, 109–122.

Bodinier, J.-L., Menzies, M.A., Thirlwall, M.F., 1991. Continental to oceanic mantle transition-REE and Sr–Nd isotopic geochemistry of the Lanzo lherzolite massif. J. Petrol. Special Volume Orogenic Lherzolites and Mantle Processes, 191–210.

Brey, G.P., Köhler, T.P., 1990. Geothermometry in four-phase lherzolite II. New thermometers and practical assessment of existing thermobarometers. J. Petrol. 31, 1353–1378.

Chapman, D.S., 1986. Thermal gradients in continental crust. In: Dawson, J.B., Carswel, D.A., Hall, J., Wadepohl, K.H. (Eds.), The Nature of the Lower Continental Crust. Geological Society Special Publication, vol. 24. Blackwell, London, pp. 63–70.

Danyushevsky, L.V., Eggins, S.M., Falloon, T.J., Christe, D.M., 2000. H_2O geochemistry in depleted to moderately enriched mid-ocean ridge magmas; Part 1: Incompatible behavior, implications for mantle storage, and origin of regional variations. J. Petrol. 41, 1329–1364.

Davies, G.F., 1999. Dynamic Earth: Plates Plumes and Mantle Convection. Cambridge University Press, Cambridge, 460 pp.

Dick, H.J.B., Bullen, T., 1984. Chromian spinel as a petrogenetic indicator in abyssal and alpine-type peridotites and spatially associated lavas. Contrib. Miner. Petrol. 86, 54–76.

Ercan, T., Satır, M., Steinitz, G., Dora, A., Sarıfakıoğlu, E., Adis, C., Walter, H.J., Yıldırım, T., 1995. Biga yarımadası ile Gökçeada, Bozcaada ve Tavşan adalarındaki (KB Anadolu) Tersiyer volkanizmasının özellikleri (Characteristics of the Tertiary volcanism in the Biga Peninsula, Gökçeada, Bozcaada and Tavşanadası, NW Anatolia). Bull. Geol. Soc. Turkey 28, 121–136.

Ford, C.E., Russell, D.G., Craven, J.A., Fisk, M.R., 1983. Olivine-liquid equilibria: temperature, pressure and composition dependence of the crystal/liquid cation partition coefficients for Mg, Fe^{2+}, Ca and Mn. J. Petrol. 24, 256–265.

Fram, M.S., Lesher, C.E., 1997. Generation and polybaric differentiation of East Greenland Early Tertiary flood basalts. J. Petrol. 38, 231–275.

Frey, F.A., Green, D.H., 1974. The mineralogy, geochemistry and origin of lherzolite inclusions in Victorian basanites. Geochim. Cosmochim. Acta 38, 1023–1059.

Frey, F.A., Prinz, M., 1978. Ultramafic inclusions from San Carlos Arizona: petrologic and geochemical data bearing on their petrogenesis. Earth Planet. Sci. Lett. 38, 129–176.

Gasparik, T., 1984. Two-pyroxene thermobarometry with new experimental data in the system CaO–MgO–Al_2O_3–SiO_2. Contrib. Miner. Petrol. 87, 87–97.

Gasparik, T., 1987. Orthopyroxene thermobarometry in simple and complex systems. Contrib. Miner. Petrol. 96, 357–370.

Ghiorso, M.S., Sack, R.O., 1995. Chemical mass transfer in magmatic processes IV A revised and internally consistent thermodynamic model for the interpolation and extrapolation of liquid–solid equilibria in magmatic systems at elevated temperatures and pressures. Contrib. Miner. Petrol. 119, 197–212.

Gök, R., Türkelli, N., Sandvol, E., Seber, D., Barazangi, M., 2000. Regional wave propagation in Turkey and surrounding regions. Geophys. Res. Lett. 27, 429–432.

Göktürkler, G., Salk, M., Sarı, C., 2003. Numerical modeling of the conductive heat transfer in western Anatolia. J. Balkan Geophys. Soc. 6, 1–15.

Green, D.H., Hibberson, W., 1970. The instability of plagioclase in peridotite at high pressure. Lithos 3, 209–321.

Griffin, W.L., O'Reilly, S.Y., Natapov, L.M., Ryan, C.G., 2003. The evolution of lithospheric mantle beneath the Kalahari Craton and its margins. Lithos 71, 215–242.

Hellebrand, E., Snow, J.E., Dick, H.J.B., Hoffmann, A.W., 2001. Coupled major and trace elements as indicators of extent of melting in mid-ocean-ridge peridotites. Nature 410, 677–681.

Hermann, W., Berry, R.F., 2002. MINSQ—a least squares spreadsheet method for calculating mineral proportions from whole rock major element analyses. Geochem. Explor. Environ. Anal. 2, 361–368.

Herzberg, C.T., 1978. Pyroxene geothermometry and geobarometry: experimental and thermodynamic evaluation of some subsolidus phase relations involving pyroxenes in the system CaO–MgO–Al_2O_3–SiO_2. Geochim. Cosmochim. Acta 42, 945–957.

Herzberg, C., Zang, J., 1996. Melting experiments on anhydrous peridotite KLB-1: compositions of magmas in the upper mantle and transition zone. J. Geophys. Res. 101, 8271–8295.

Herzberg, C., O'Hara, M.J., 2002. Plume associated ultramafic magmas of Phanerozoic age. J. Petrol. 43, 1857–1883.
Herzberg, C., Raterron, P., Jianzhong Z., 2000. New experimental observations on the anhydrous solidus for peridotite KLB-1. Geochem. Geophys. Geosyst. 1, 2000GC000089, 1–15.
Henjes-Kunst, F., Altherr, R., 1992. Metamorphic petrology of xenoliths from Kenya and Northern Tanzania and implications for geotherms in lithospheric structure. J. Petrol. 33, 1125–1156.
Hirose, K., Kushiro, I., 1993. Partial melting of dry peridotites at high pressures: determination of composition of melts segregated from peridotite using aggregate of diamond. Earth Planet. Sci. Lett. 114, 477–489.
Horasan, G., Gulen, L., Pinar, A., Kalafat, D., Ozel, N., Kuleli, H.S., Isikara, A.M., 2002. Lithospheric structure of the Marmara and Aegean Regions, Western Turkey. Bull. Seismol. Soc. Am. 91, 322–329.
Ilkisik, O.M., 1995. Regional heat flow in western Anatolia using silica temperature estimates from thermal springs. Tectonophysics 244, 175–184.
Ionov, D.A., O'Reilly, S.Y., Griffin, W.L., 1998. A geotherm and lithospheric section for central Mongolia (Tariat Region). In: Flower, M.F.J., Chung, S.-L., Lo, C.-H., Lee, T.-Y. (Eds.), Mantle Dynamics and Plate Interaction in East Asia. American Geophysical Union, Geodynamic Series, vol. 27, pp. 127–153.
Kelemen, P.B., Dick, H.J.B., Quick, J.E., 1992. Formation of harzburgite by pervasive melt/rock reaction. Nature 358, 635–641.
Klemme, S., O'Neill, H.St.C., 2000. The near-solidus transition from garnet lherzolite to spinel lherzolite. Contrib. Miner. Petrol. 138, 237–248.
Köhler, T.P., Brey, G.P., 1990. Calcium exchange between olivine and clinopyroxene calibrated as a geobarometer for natural peridotites from 2 to 60 kbar with applications. Geochim. Cosmochim. Acta 54, 2375–2388.
Kushiro, I., 1998. Compositions of partial melts formed in mantle peridotites at high pressures and their relations to those of primitive MORB. Phys. Earth Planet. Interiors 107, 110–113.
Libourel, G., 1999. Systematics of calcium partitioning between olivine and silicate melt: implications for melt structure and calcium content of magmatic olivines. Contrib. Miner. Petrol. 136, 63–80.
Maaloe, S., Aoki, K., 1977. The major element composition of the upper mantle estimated from the composition of lherzolites. Contrib. Miner. Petrol. 63, 161–173.
McDonough, W.F., Sun, S.-s., 1995. The composition of the earth. Chem. Geol. 120, 223–253.
McKenzie, D.P., Bickle, M.J., 1988. The volume and composition of melt generated by extension of the lithosphere. J. Petrol. 29, 627–679.
McKenzie, D.P., O'Nions, R.K., 1991. Partial melt distribution from inversion of rare earth element concentrations. J. Petrol. 32, 1021–1991.
Mercier, J.-C., 1980. Single pyroxene thermobarometry. Tectonophysics 70, 1–37.
Mercier, J.-C., Nicolas, A., 1975. Textures and fabrics of upper mantle peridotites as illustrated by xenoliths from basalts. J. Petrol. 16, 454–487.
Mooney, W.D., Braile, L.W., 1989. The seismic structure of the continental crust and upper mantle of North America. In: Bally, A.W., Palmer, A.R. (Eds.), Geology of North America—An Overview. Geological Society of America, pp. 39–52.
Morimonto, N., 1989. Nomenclature of pyroxenes. Can. Mineral. 27, 143–156.
Nicolas, A., Lucazeau, F., Bayer, R., 1987. Peridotite xenoliths in Massif Central basalts France: textural and geophysical evidence for asthenospheric diapirism. In: Nixon, P.H. (Ed.), Mantle Xenoliths. John Wiley, New York, pp. 563–574.
Obata, M., 1976. The solubility of Al_2O_3 in orthopyroxenes in spinel and plagioclase peridotites and spinel pyroxenite. Am. Mineral. 61, 804–816.
O'Neill, H.St.C., 1981. The transition between spinel lherzolite and garnet lherzolite, and its use as geobarometer. Contrib. Miner. Petrol. 77, 251–255.
O'Reilly, S.Y., Griffin, W.L., 1985. A xenolith derived geotherm for Southeastern Australia and its geophysical implications. Tectonophysics 111, 41–64.
Panagiotopoulos, D.G., Papazacos, B.C., 1985. Travel times of Pn-waves in the Aegean and surrounding area. Geophys. J. R. Astronom. Soc. 80, 165–176.
Pearce, J.A., Barker, P.F., Edwards, S.J., Parkinson, I.J., Leat, P.T., 1999. Geochemistry and tectonic significance of peridotites from the South Sandwich arc-basin systems South Atlantic. Contrib. Miner. Petrol. 139, 36–53.
Perinçek, D., 1991. Possible strand of the North Anatolian fault in the Thrace Basin Turkey: an interpretation. AAPG Bull. 75, 241–257.
Pfister, M., Rybach, L., Şimsek, Ş., 1998. Geothermal reconnaissance of the Sea of Marmara region (NW Turkey): surface heat flow density in the area of active continental extension. Tectonophysics 291, 77–89.

Pollack, H.N., Chapman, D.S., 1977. On the regional variation of heat flow, geotherms and lithospheric thickness. Tectonophysics 38, 279–296.
Reid, A.M., Dawson, J.B., 1972. Olivine-garnet reaction in peridotites from Tanzania. Lithos 5, 115–124.
Roeder, P.L., Emslie, R.F., 1970. Olivine-liquid equilibrium. Contrib. Miner. Petrol. 29, 275–289.
Rudnick, R.L., McDonough, W.F., O'Connell, R.J., 1998. Thermal structure, thickness and composition of continental lithosphere. Chem. Geol. 145, 395–411.
Sachtleben, T.H., Seck, H.A., 1981. Chemical control on the Al-solubility in orthopyroxene and its implications on pyroxene thermometer. Contrib. Miner. Petrol. 78, 157–165.
Saunders, P., Priestley, K., Taymaz, T., 1998. Variation in the crustal structure beneath western Turkey. Geophys. J. Int. 134, 373–389.
Seyler, M., Bonatti, E., 1994. Na, Al^4 and Al^6 in clinopyroxenes of continental and suboceanic ridge peridotites: a clue to different melting processes in the mantle? Earth Planet. Sci. Lett. 122, 281–289.
Smith, D., 1977. The origin and interpretation of spinel-pyroxene in peridotite. J. Geol. 85, 476–482.
Song, Y., Frey, F.A., 1989. Geochemistry of peridotite xenoliths in basalts from Hannuoba Eastern China: implications for subcontinental mantle heterogeneity. Geochim. Cosmochim. Acta 53, 97–113.
Stern, C.R., Killian, R., Olker, B., Hauri, E.H., Kyser, T.K., 1999. Evidence from mantle xenoliths for relatively thin (<100 km) continental lithosphere below the Phanerozoic crust of southernmost South America. Lithos 48, 217–235.
Thompson, R.N., Gibson, S.A., 2000. Transient high temperatures in mantle plume heads inferred from magnesian olivines in Phanerozoic picrites. Nature 407, 502–506.
Tracy, R.J., 1980. Petrology and genetic significance of an ultramafic xenolith suite from Tahiti. Earth Planet. Sci. Lett. 48, 80–96.
Turgut, S., Türkaslan, M., Perinçek, D., 1991. Evolution of the Thrace sedimentary basin and hydrocarbon prospectivity. In: Spencer, A.M. (Ed.), Generation, Accumulation and Production of Europe's Hydrocarbon, vol. 1. European Association of Petroleum Geosciences Special Publication, pp. 415–437.
Ulmer, P., 1989. The dependence of Fe^{2+}–Mg cation partitioning between olivine and basaltic liquid on pressure, temperature and composition: an experimental study to 30 kbars. Contrib. Miner. Petrol. 101, 261–273.
Webb, S.A., Wood, B.J., 1986. Spinel–pyroxene–garnet relationships and their dependencies on Cr/Al ratios. Contrib. Miner. Petrol. 92, 471–480.
Wells, P.R.A., 1977. Pyroxene thermometry in simple and complex systems. Contrib. Miner. Petrol. 62, 129–139.
Werling, F., Altherr, R., 1997. Thermal evolution of the lithosphere beneath the French Massif Central as deduced from geothermobarometry on mantle xenoliths. Tectonophysics 275, 119–141.
Witt-Eickschein, G., Seck, H.A., 1991. Solubility of Ca and Al in orthopyroxene from spinel peridotite: an improved version of an empirical geothermometer. Contrib. Miner. Petrol. 106, 431–439.
Wood, B.J., 1990. Oxygen barometry of spinel peridotites. In: Lindsley, D.H., (Ed.), Mineralogical Society of America. Rev. Mineral. 25, 417–431.
Wood, B.J., Banno, S., 1973. Garnet-orthopyroxene and orthopyroxene-clinopyroxene relationships in simple and complex systems. Contrib. Miner. Petrol. 42, 109–124.
Xu, X.S., O'Reilly, S.Y., Zhou, X.H., Griffin, W.L., 1996. A xenolith-derived crustal geotherm and the crust-mantle boundary at Qiling, Southeastern China. Lithos 38, 41–62.
Xu, Y.G., Menzies, M.A., Vroon, P., Mercier, J.-C., Lin, C.Y., 1998. Texture–temperature–geochemistry relationship in the upper mantle as revealed from spinel peridotite xenoliths from Wangqing, NE China. J. Petrol. 39, 469–493.
Yilmaz, Y., Polat, A., 1998. Geology and evolution of the thrace volcanism Turkey. Acta Vulcanol. 10, 293–303.